Short article

Cell Host & Microbe

Broad receptor tropism and immunogenicity of a clade 3 sarbecovirus

Graphical abstract

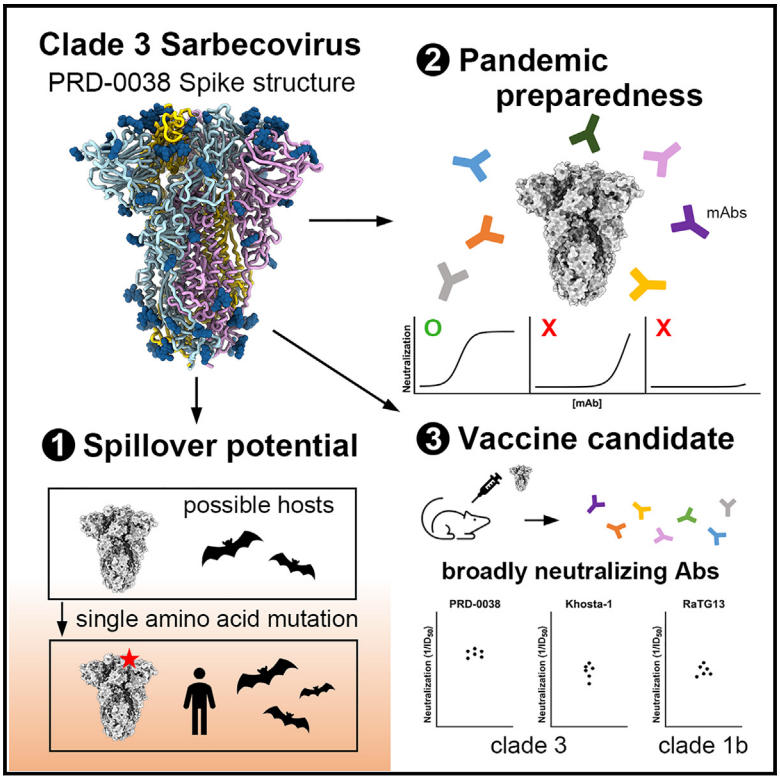

Authors

Jimin Lee, Samantha K. Zepeda, Young-Jun Park, ..., Neil P. King, Tyler N. Starr, David Veesler

Correspondence

dveesler@uw.edu

In brief

Lee and colleagues show that the PRD-0038 clade 3 sarbecovirus spike has broad ACE2 receptor usage that can be expanded by mutations. Structural and serological studies explain receptor tropism, identify PRD-0038 cross-neutralizing antibodies, and demonstrate that the PRD-0038 spike elicits more broadly reactive sarbecovirus antibodies than the SARS-CoV-2 spike.

Highlights

- PRD-0038 clade 3 sarbecovirus spike has a broad ACE2 receptor usage
- RBD mutations expand tropism to additional *Rhinolophus* ACE2s and to human ACE2
- Cryo-EM blueprints explain receptor tropism and spike antigenicity
- Identification of PRD-0038 cross-neutralizing antibodies for pandemic preparedness

Lee et al., 2023, Cell Host & Microbe *31*, 1961–1973
December 13, 2023
https://doi.org/10.1016/j.chom.2023.10.018

CellPress

Cell Host & Microbe

CellPress
OPEN ACCESS

Short article

Broad receptor tropism and immunogenicity of a clade 3 sarbecovirus

Jimin Lee,[1,6] Samantha K. Zepeda,[1,6] Young-Jun Park,[1,2] Ashley L. Taylor,[3] Joel Quispe,[1] Cameron Stewart,[1] Elizabeth M. Leaf,[1,4] Catherine Treichel,[1,4] Davide Corti,[5] Neil P. King,[1,4] Tyler N. Starr,[3] and David Veesler[1,2,7,*]

[1]Department of Biochemistry, University of Washington, Seattle, WA, USA
[2]Howard Hughes Medical Institute, Seattle, WA 98195, USA
[3]Department of Biochemistry, University of Utah School of Medicine, Salt Lake City, UT 84112, USA
[4]Institute for Protein Design, University of Washington, Seattle, WA 98195, USA
[5]Humabs Biomed SA, a Subsidiary of Vir. Biotechnology, 6500 Bellinzona, Switzerland
[6]These authors contributed equally
[7]Lead contact
*Correspondence: dveesler@uw.edu
https://doi.org/10.1016/j.chom.2023.10.018

SUMMARY

Although *Rhinolophus* bats harbor diverse clade 3 sarbecoviruses, the structural determinants of receptor tropism along with the antigenicity of their spike (S) glycoproteins remain uncharacterized. Here, we show that the African *Rhinolophus* bat clade 3 sarbecovirus PRD-0038 S has a broad angiotensin-converting enzyme 2 (ACE2) usage and that receptor-binding domain (RBD) mutations further expand receptor promiscuity and enable human ACE2 utilization. We determine a cryo-EM structure of the PRD-0038 RBD bound to *Rhinolophus alcyone* ACE2, explaining receptor tropism and highlighting differences with SARS-CoV-1 and SARS-CoV-2. Characterization of PRD-0038 S using cryo-EM and monoclonal antibody reactivity reveals its distinct antigenicity relative to SARS-CoV-2 and identifies PRD-0038 cross-neutralizing antibodies for pandemic preparedness. PRD-0038 S vaccination elicits greater titers of antibodies cross-reacting with vaccine-mismatched clade 2 and clade 1a sarbecoviruses compared with SARS-CoV-2 S due to broader antigenic targeting, motivating the inclusion of clade 3 antigens in next-generation vaccines for enhanced resilience to viral evolution.

INTRODUCTION

Two sarbecoviruses have crossed the species barrier and spilled over to humans in the past two decades. SARS-CoV-1 emerged in 2002 and spread worldwide through air travel routes, leading to an epidemic with 8,098 cases and 774 deaths.[1,2] SARS-CoV-2 emerged at the end of 2019 and led to the devastating COVID-19 pandemic that claimed millions of lives worldwide.[3,4] Both viruses enter human cells via spike (S)-mediated fusion of the viral and host membranes upon binding to the angiotensin-converting enzyme 2 (ACE2) receptor.[3,5–8]

Reports of additional sarbecovirus spillovers to humans[9,10] along with detection of numerous sarbecoviruses in bats and other wild animals[3,11–16] underscore the recurrent zoonotic threat to public health posed by these viruses. The S glycoprotein of some of these sarbecoviruses harbors a receptor-binding domain (RBD) that utilizes the human ACE2 receptor to enter host cells, indicating that they could possibly cross the species barrier to infect humans.[6,12,17–20]

Phylogenetic classification of sarbecoviruses based on their RBD sequences led to the definition of at least four clades: clade 1a (e.g., SARS-CoV-1), clade 1b (e.g., SARS-CoV-2), clade 2 (e.g., RmYN02), and clade 3 (e.g., BtKY72).[21,22] Clade 3 sarbecoviruses have been identified in bats in Europe and Africa,[23–28] such as BtKY72 and PRD-0038 for which sequences were found in Kenya and Rwanda, respectively. We recently showed that the S glycoprotein of one of them (BtKY72) could utilize two *Rhinolophus affinis* (*R. affinis*) ACE2 alleles to promote entry into cells.[29] Furthermore, two amino acid residue substitutions in the BtKY72 RBD enabled S-mediated entry into human ACE2-expressing cells, broadening the range of sarbecoviruses with spillover potential.[29] The importance of this observation was further underscored by the recent discovery of the clade 3 Khosta-2 virus,[28] which independently acquired the ability to bind[29] and enter cells[30] using the human ACE2 receptor. Studying the structure and functional properties of clade 3 sarbecovirus S glycoproteins is therefore crucial to understand spillover risk and assist in pandemic preparedness.

Here, we report that the S glycoprotein of the clade 3 sarbecovirus PRD-0038, which is a member of the largely uncharacterized African bat-borne sarbecoviruses, has a broad ACE2 usage and that PRD-0038 RBD mutations further expand entry receptor tropism to additional *Rhinolophus* bat species and human ACE2. We determined structures of the PRD-0038 RBD bound to *Rhinolophus alcyone* (*R. alcyone*) ACE2 and of the PRD-0038 S trimer,

explaining receptor tropism and the distinct antigenicity of clade 3 sarbecoviruses relative to SARS-CoV-2 and SARS-CoV-1. Evaluation of a panel of monoclonal antibodies enabled identification of PRD-0038 cross-neutralizing antibodies that could be deployed for outbreak response. Vaccination of mice with PRD-0038 S elicited greater titers of antibodies cross-reacting with vaccine-mismatched clade 2 and clade 1a sarbecoviruses, relative to SARS-CoV-2 S immunization, indicating that addition of clade 3 antigens in vaccine formulations could enhance the resilience of antibody responses to viral evolution. Our findings highlight a molecular pathway for possible zoonotic spillover of a clade 3 sarbecovirus and the necessity of developing pan-sarbecovirus vaccines and countermeasures.

RESULTS

PRD-0038 S can utilize a broad spectrum of *Rhinolophus* bat ACE2 orthologs as entry receptors

To investigate the promiscuity of clade 3 sarbecovirus host receptor usage, we first assessed binding of a panel of *Rhinolophus* bat ACE2 orthologs harboring a C-terminal human Fc fusion to the immobilized PRD-0038 RBD using biolayer interferometry (BLI) (Figures 1A and 1B). We selected PRD-0038 as a representative member of African bat-borne sarbecoviruses due to its more ancestral phylogenetic positioning relative to the other two sarbecoviruses isolated on the same continent[29] (BtKY72 and PDF-2370) and the high sequence similarity of their S glycoproteins. Our ACE2 panel comprised eight distinct *Rhinolophus sinicus* (*R. sinicus*) alleles and two distinct *R. affinis* alleles, which were defined based on polymorphisms within the region recognized by sarbecovirus RBDs,[29,31] as well as *R. alcyone* and *Rhinolophus landeri* (*R. landeri*) orthologs. *R. sinicus* Asian bats are probable reservoir hosts for SARS-CoV-1,[14] *R. affinis* bats have been shown to host closely related viruses to SARS-CoV-2,[3] whereas *R. alcyone* and *R. landeri* bats are found in sub-Saharan Africa, overlapping with the regions of sampling of several clade 3 sarbecoviruses (the exact *Rhinolophus* species from which PRD-0038 and BtKY72 have been sampled is unknown)[24,25] (Figure 1C). We observed the strongest binding to the PRD-0038 RBD with *R. alcyone* ACE2, which exhibited the slowest dissociation kinetics in our panel (Figure 1A). The PRD-0038 RBD also interacted with both *R. affinis* ACE2s, albeit more tightly with the 9479 allele than the 787 allele, and with *R. landeri* ACE2 (Figure 1A). Finally, we detected binding to four out of the eight *R. sinicus* alleles evaluated (Figure 1B).

To further evaluate receptor tropism, we pseudotyped vesicular stomatitis virus (VSV) particles with PRD-0038 S and assessed entry into HEK293T cells transiently transfected with the corresponding set of full-length, membrane-anchored ACE2s (Figure 1D). Concurring with our binding data, *R. alcyone* enabled robust entry of PRD-0038 S VSV (Figure 1D), in line with a previous study.[32] Moreover, we also detected efficient entry into cells expressing *R. affinis* 9479 and 787 ACE2 alleles, *R. landeri* ACE2, and the four *R. sinicus* ACE2 alleles for which binding was detected by BLI (Figure 1D). Collectively, these data show that PRD-0038 S recognizes and can utilize a broad spectrum of *Rhinolophus* bat ACE2 orthologs as entry receptors, including those from bat species known to be found in geographic areas proximal to the site of PRD-0038 discovery.

Molecular basis of PRD-0038 RBD engagement of the *R. alcyone* ACE2 receptor

To reveal the structural determinants of ACE2 recognition by clade 3 sarbecoviruses, we determined a reconstruction of the PRD-0038 RBD bound to the natively dimeric *R. alcyone* ACE2 (RaACE2) ectodomain using single-particle cryoelectron microscopy (cryo-EM) (Figures 1E and S1; Table S2). Symmetry expansion and local refinement yielded a structure at 3.2 Å resolution of the ACE2 peptidase domain bound to the RBD revealing the molecular interactions mediating complex formation. An average surface of ~750 Å^2 is buried at the ACE2/RBD interface as compared with ~840 Å^2 for the complexes of human ACE2 (hACE2) bound to the SARS-CoV-2 RBD[33] or to the SARS-CoV-1 RBD.[34] The relative orientation of the binding partners is similar for these three structures, likely due to the conservation of several key ACE2-interacting residues including $L444_{PRD-0038}$/$L455_{SARS-CoV-2}$ and $F445_{PRD-0038}$/$F456_{SARS-CoV-2}$, $L475_{PRD-0038}$/$L472_{SARS-CoV-1}$, $Y478_{PRD-0038}$/$Y489_{SARS-CoV-2}$/$Y475_{SARS-CoV-1}$, $G485_{PRD-0038}$/$G496_{SARS-CoV-2}$/$G482_{SARS-CoV-1}$, $G491_{PRD-0038}$/$G502_{SARS-CoV-2}$/$G488_{SARS-CoV-1}$, and $Y494_{PRD-0038}$/$Y505_{SARS-CoV-2}$/$Y491_{SARS-CoV-1}$ (Figures 1F–1I). However, the salt bridge formed between $K417_{SARS-CoV-2}$ and $D30_{hACE2}$ is absent due to substitution to $V408_{PRD-0038}$ and $V404_{SARS-CoV-1}$ (Figures 1F, 1G, and 1J). Furthermore, the electrostatic interactions involving residues $D38_{hACE2}$ and $Q42_{hACE2}$ with $Y449_{SARS-CoV-2}$ and $Q498_{SARS-CoV-2}$ or $Y436_{SARS-CoV-1}$ and $Y484_{SARS-CoV-1}$ are lost due to truncation and remodeling of the PRD-0038 433–440 loop along with substitution of $Q498_{SARS-CoV-2}$ to $T487_{PRD-0038}$ (Figures 1F–1H, 1K, and S2). The interface between $T500$/$N501_{SARS-CoV-2}$ (or Y501 in currently circulating variants) and $Y41_{hACE2}$ is replaced by tenuous contacts between the topologically equivalent residues $T489$/$V490_{PRD-0038}$ and $H41_{RaACE2}$ (Figures 1F, 1G, and 1K). $Q493_{SARS-CoV-2}$ optimally interacts with $K31_{hACE2}$/$E35_{hACE2}$, whereas the topologically equivalent residue $K482_{PRD-0038}$ is better adapted to $N31_{RaACE2}$/$E35_{RaACE2}$ due to swapping of the position of a positively charged amino acid side chain across the interface (Figures 1F, 1G, and 1L). These findings concur with (1) the enhanced entry of the closely related BtKY72 RBD-harboring pseudovirus into cells expressing a human ACE2 K31D mutant relative to wild-type ACE2[32]; (2) the isolation of a mouse-adapted SARS-CoV-2 isolate harboring the Q493K substitution[35] that promotes favorable interactions with mouse ACE2, the latter ortholog also possessing residues N31/E35[36,37]; and (3) the emergence of $R493_{SARS-CoV-2}$ in Omicron BA.1 and BA.2,[36,37] which was subsequently reverted to the more favorable $Q493_{SARS-CoV-2}$ in subsequent variants, likely due to relieving electrostatic repulsion with $K31_{hACE2}$.[38] Overall, most of the PRD-0038 RBD binding interface with *R. alcyone* ACE2 is remodeled as compared with human ACE2 bound to SARS-CoV-2 or SARS-CoV-1, thereby explaining the shift in receptor species tropism.

PRD-0038 RBD mutations enable human ACE2 utilization and expand receptor tropism to additional geographically relevant bat species

To investigate how viral evolution could alter the PRD-0038 receptor species tropism for pandemic preparedness, we evaluated the impact of RBD mutations on utilization of several ACE2 orthologs. Using BLI, we observed that human ACE2-Fc

CellPress
OPEN ACCESS

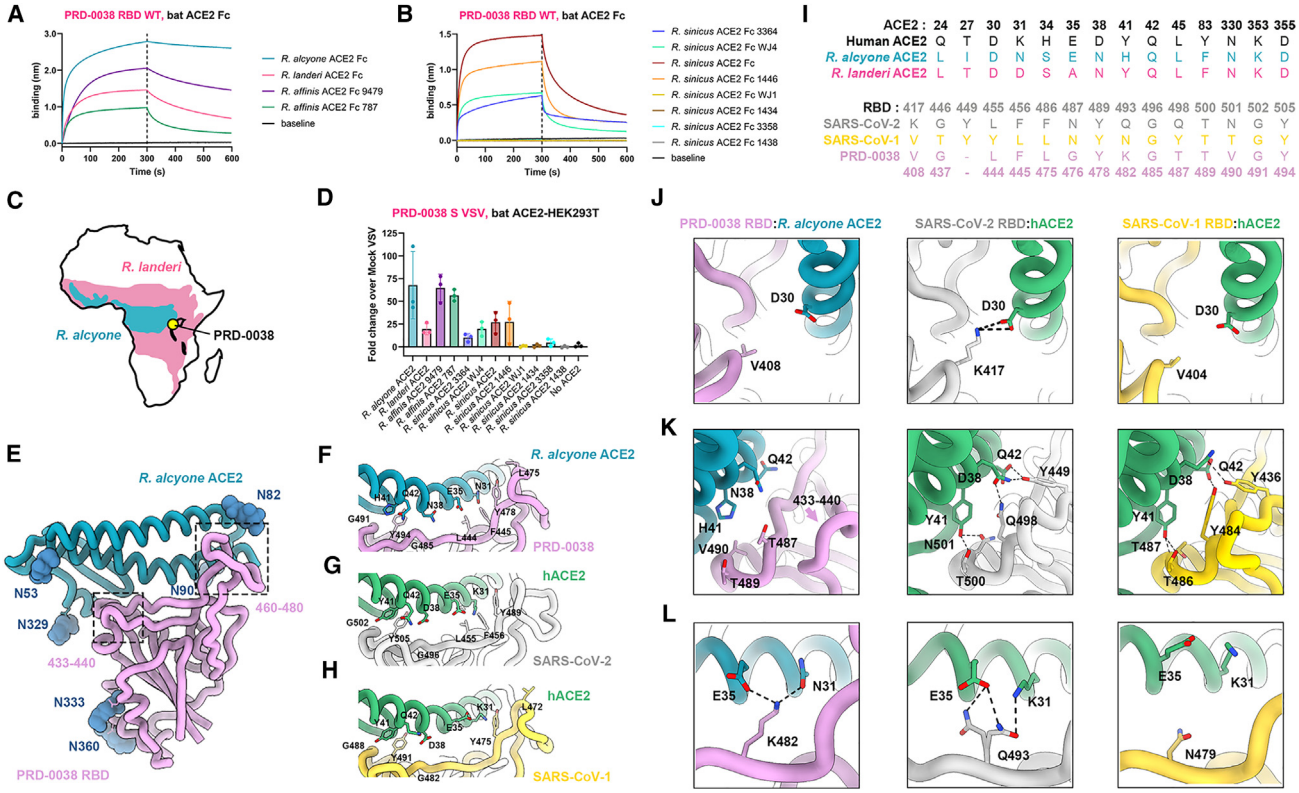

Figure 1. The clade 3 PRD-0038 sarbecovirus has a broad *Rhinolophus* bat ACE2 tropism

(A and B) BLI binding analysis of *R. affinis*, *R. alcyone*, and *R. landeri* (see also Table S1) (A) or *R. sinicus* (B) ACE2-Fc alleles at a concentration of 1 μM to the biotinylated PRD-0038 RBD immobilized on streptavidin biosensors. Baselines represent non-specific binding of uncoated streptavidin biosensors to 0.25 μM ACE2 Fc.

(C) Known geographic distribution of *R. alcyone* and *R. landeri* bats in sub-Saharan Africa (https://www.iucnredlist.org/). The yellow area indicates the site of PRD-0038 sampling (Rwanda).

(D) Entry of VSV pseudotyped with wild-type PRD-0038 S in HEK293T cells transiently transfected with the indicated *Rhinolophus* bat ACE2 orthologs. Each point represents the average of technical duplicates from each biological triplicate. Means and standard deviations shown as bars and error bars.

(E) Cryo-EM structure of the PRD-0038 RBD bound to *R. alcyone* ACE2. N-linked glycans are shown as dark blue spheres and labeled with the corresponding asparagine residue number. The dotted gray boxes highlight regions with major structural deviations from SARS-CoV-2 (see also Figure S2).

(F–H) Close-up views of the interface between the PRD-0038 RBD and *R. alcyone* ACE2 (F, pink and blue, respectively), the SARS-CoV-2 RBD and human ACE2 (G, gray and green, respectively, PDB: 6M0J[33]), and the SARS-CoV-1 RBD and human ACE2 (H, gold and green, respectively, PDB: 2AJF[34]). Key conserved residues at the interface are rendered as sticks.

(I) Sequence alignments of the key ACE2 and RBD residues at the binding interfaces. Numberings used are for human ACE2 (black), SARS-CoV-2 (gray), and PRD-0038 (pink) (see also Table S1).

(J–L) Close-up views of selected key contact residues at the interface between the PRD-0038 RBD and *R. alcyone* ACE2, the SARS-CoV-2 RBD and human ACE2, and the SARS-CoV-1 RBD and human ACE2 colored as in (F). (J) shows that the salt bridge formed between $K417_{SARS\text{-}CoV\text{-}2}$ and $D30_{hACE2}$ is absent due to substitution to $V408_{PRD\text{-}0038}$ and $V404_{SARS\text{-}CoV\text{-}1}$. (K) shows that the electrostatic interactions involving residues $D38_{hACE2}$ and $Q42_{hACE2}$ with $Y449_{SARS\text{-}CoV\text{-}2}$ and $Q498_{SARS\text{-}CoV\text{-}2}$ or $Y436_{SARS\text{-}CoV\text{-}1}$ and $Y484_{SARS\text{-}CoV\text{-}1}$ are lost due to truncation and remodeling of the PRD-0038 433–440 loop along with substitution of $Q498_{SARS\text{-}CoV\text{-}2}$ to $T487_{PRD\text{-}0038}$ (L) shows that $Q493_{SARS\text{-}CoV\text{-}2}$ optimally interacts with $K31_{hACE2}$/$E35_{hACE2}$, whereas the topologically equivalent residue $K482_{PRD\text{-}0038}$ is better adapted to $N31_{RaACE2}$/$E35_{RaACE2}$ due to swapping of the position of a positively charged amino acid side chain across the interface.

did not bind to the wild-type PRD-0038 RBD (Figure 2A). However, we found that two amino acid residue substitutions promoted binding of human ACE2-Fc to the immobilized PRD-0038 K482Y/T487W RBD mutant (Figure 2A, SARS-CoV-2 numbering 493Y/498W),[29] in line with their ability to enable BtKY72 S-mediated utilization of human ACE2.[29] Moreover, we found that human ACE2-Fc interacted with the T487W RBD, albeit weakly (Figure 2A). We validated these findings using deep mutational scanning (DMS) of the yeast-displayed PRD-0038 RBD showing that T487W is the only single amino acid mutation enabling detection of human ACE2-Fc binding (Figures 2B and S3). The geographically relevant *R. alcyone* and *R. landeri* ACE2 orthologs exhibited enhanced binding to the PRD-0038 T487W RBD relative to the wild-type RBD, with 1:1 binding affinity improvements corresponding to 2- and greater than 1 order of magnitude, respectively (Figures 2C and 2D; Table S3). These data concur with our DMS measurements showing that T487W mutation had the most marked positive effect on *R. landeri* ACE2 binding (Figures 2B and S3). Furthermore, the PRD-0038 T487W RBD mutation enhanced binding to the *R. affinis* 787 allele as well as to the *R. sinicus* alleles recognized by the wild-type PRD-0038 RBD and enabled detectable binding to the

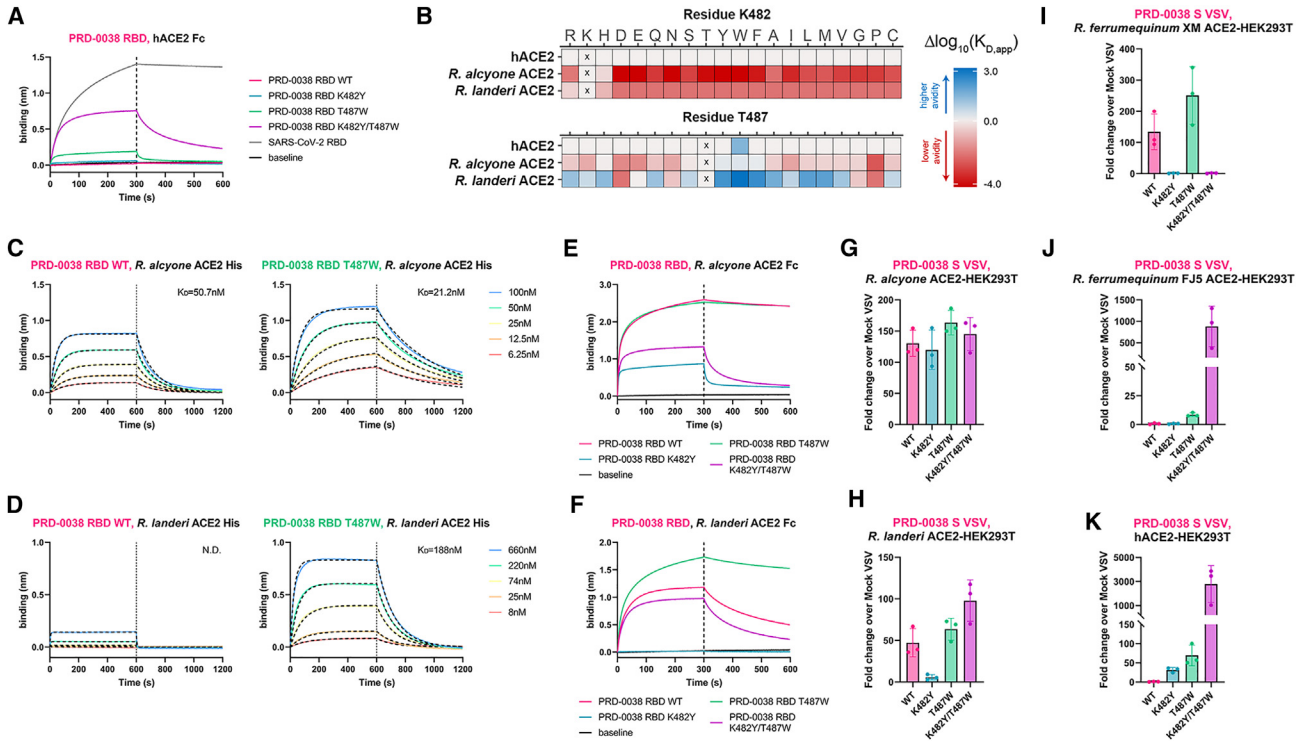

Figure 2. PRD-0038 RBD amino acid mutations broaden receptor tropism

(A) BLI binding analysis of 1 μM dimeric hACE2-Fc to biotinylated wild-type and mutant PRD-0038 RBDs immobilized on streptavidin biosensors.

(B) DMS heatmaps of change in binding avidity to several ACE2-Fc orthologs caused by all possible mutations of the PRD-0038 RBD residues K482 and T487. An interactive version of the DMS data can be found at https://tstarrlab.github.io/SARSr-CoV-RBD_DMS/RBD-heatmaps_delta/.

(C) BLI binding analysis of various concentrations of monomeric *R. alcyone* ACE2 to biotinylated wild-type (left) and T487W (right) PRD-0038 RBDs immobilized on streptavidin biosensors.

(D) BLI binding analysis of various concentrations of monomeric *R. landeri* ACE2 to biotinylated wild-type (left) and T487W (right) PRD-0038 RBDs immobilized on streptavidin biosensors.

(E) BLI binding analysis of 1 μM dimeric *R. alcyone* ACE2-Fc to biotinylated wild-type and mutant PRD-0038 RBDs immobilized on streptavidin biosensors.

(F) BLI binding analysis of 1 μM dimeric *R. landeri* ACE2-Fc to biotinylated wild-type and mutant PRD-0038 RBDs immobilized on streptavidin biosensors.

(G–K) Entry of VSV pseudotyped with wild-type and mutants PRD-0038 S into HEK293T cells transiently transfected with *R. alcyone* ACE2 (G), *R. landeri* ACE2 (H), *R. ferrumequinum* XM_033107295.1 (I, XM), *R. ferrumequinum* FJ598617.1 (J, FJ5), or stably expressing human ACE2 (K). Each point represents the average of technical triplicates from each biological triplicate. Means and standard deviations shown as bars and error bars.

See STAR Methods and Figure S4E for VSV S pseudotype normalization details.

R. sinicus WJ1 allele (Figures S4A and S4B). By contrast, the K482Y mutation was deleterious for binding to *R. alcyone*, *R. landeri*, *R. affinis*, and *R. sinicus* ACE2 orthologs (Figures 2E, 2F, S3, S4C, and S4D). We observed that wild-type PRD-0038 S and all three mutants (K482Y, T487W, and K482Y/T487W) promoted entry of VSV pseudotypes in HEK293T cells transiently transfected with *R. alcyone* ACE2 or with *R. landeri* ACE2 except for PRD-0038 K482Y S VSV that did not enter *R. landeri* ACE2-expressing cells (Figures 2G, 2H, and S4E), suggesting that binding avidity could overcome to some extent the observed differences in affinity. To broaden our understanding of PRD-0038 tropism, we also examined cell entry promoted by transient transfection of ACE2 alleles from *Rhinolophus ferrumequinum* (*R. ferrumequinum*) bats, which are found in northern Africa, southern Europe, and southeast Asia. We observed that *R. ferrumequinum* ACE2 allele XM_033107295.1 promoted entry of wild-type and T487W PRD-0038 S VSV, whereas *R. ferrumequinum* ACE2 allele FJ598617.1 enabled entry of T487W and even more so of K482Y/T487W PRD-0038 S VSV (Figures 2I and 2J). Finally, we observed entry of PRD-0038 T487W S and even more so of PRD-0038 K482Y/T487W S VSV pseudoviruses in HEK293T cells stably expressing human ACE2 (Figure 2K). These findings indicate that a single RBD residue mutation is sufficient for broadening the *Rhinolophus* bat ACE2 tropism and for enabling PRD-0038 S-mediated entry into cells overexpressing the human ACE2 receptor, highlighting the possible future zoonotic risk of this virus and related clade 3 sarbecoviruses.

Architecture of the PRD-0038 S trimer

To unveil the three-dimensional (3D) organization of the clade 3 sarbecovirus infection machinery, we determined the structure of prefusion PRD-0038 S using single-particle cryo-EM. After 3D classification and refinement, we obtained a 2.8 Å resolution reconstruction (Figures 3A, 3B, 3C, and S5; Table S2) of the trimer with the three RBDs in the closed conformation applying C3 symmetry, as we did not detect particle images corresponding to S trimers with open RBD conformations (Figure S5). We used local refinement to improve the resolution of the N-terminal

CellPress
OPEN ACCESS

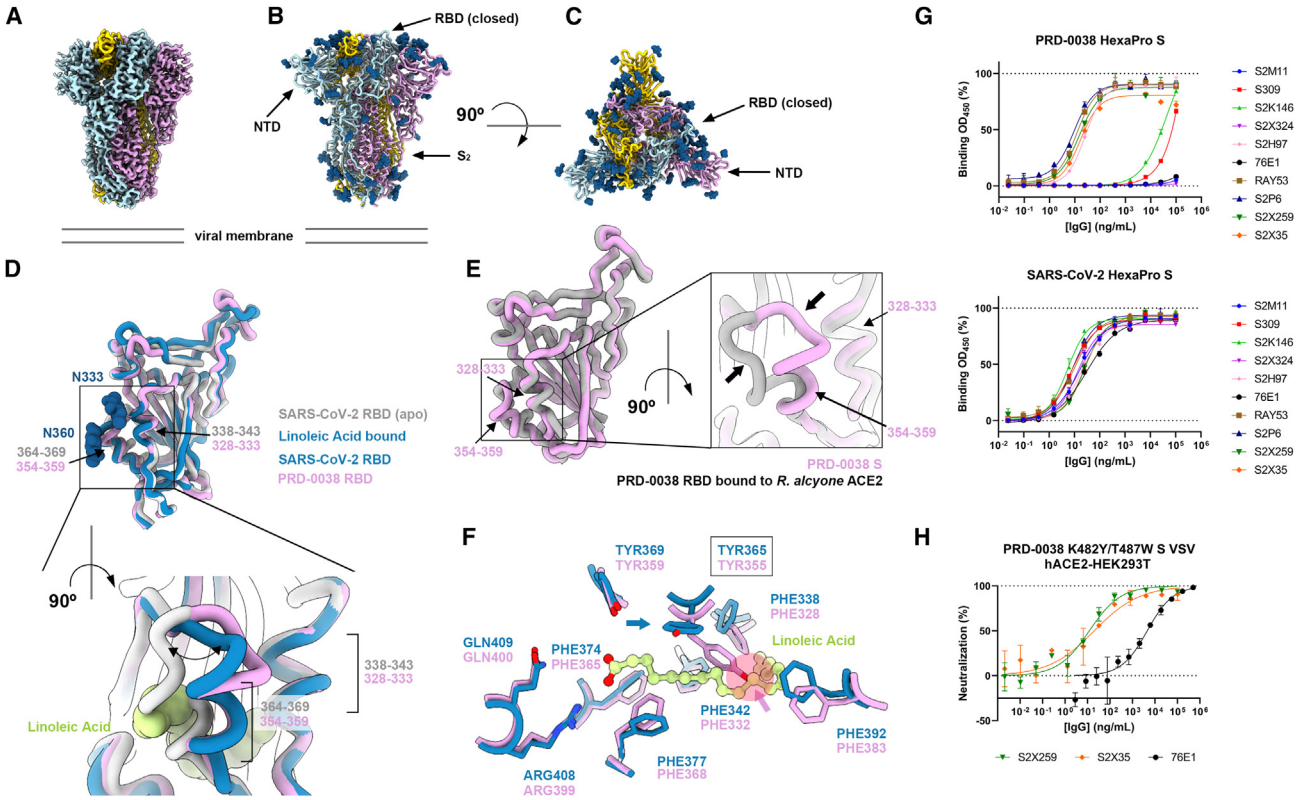

Figure 3. Architecture and antigenicity of the PRD-0038 S trimer

(A) Unsharpened cryo-EM map of the closed PRD-0038 S trimer at 2.8 Å resolution.

(B and C) Ribbon diagram of the PRD-0038 S trimer atomic model viewed along (B, side) and normal (C, top) to the viral membrane. N-linked glycans are rendered as blue spheres. In panels (A–C), S protomers are colored blue, pink, and gold.

(D) Superimposition of the PRD-0038 S structure described here to the apo (gray, PDB: 6VXX[5]) and linoleic acid-bound (blue, PDB: 6ZB5[44]) SARS-CoV-2 S structures with a close-up view of the linoleic acid-binding pocket. N-linked glycans at positions N333 and N360 are rendered as blue spheres.

(E) Superimposition of the PRD-0038 RBDs from the apo S structure (pink) and from the *R. aclyone* ACE2-bound RBD structure (gray).

(F) Conservation of the SARS-CoV-2 linoleic acid-binding residues in PRD-0038 S. The PRD-0038 S Y355 side chain rotamer (Y365 in SARS-CoV-2 numbering) would sterically hinder linoleic acid binding (semi-transparent red circle denoted with an arrow).

(G) Evaluation of binding of a panel of monoclonal antibodies to PRD-0038 S Hexapro S and SARS-CoV-2 Hexapro S measured by ELISA. Each point represents the mean of technical triplicates. Standard deviations shown as error bars.

(H) Monoclonal antibody-mediated neutralization of PRD-0038 K482Y/T487W S pseudotyped VSV entry into HEK293T cells stably expressing human ACE2. Each point represents the mean of technical duplicates. Standard deviations shown as error bars.

domain (NTD) within the S trimer yielding a map at 2.9 Å resolution (Figure S5). The final model contains residues 18–1,125 with chain breaks between residues 667–673 and 812–830.

The overall architecture of the PRD-0038 S trimer is similar to that of SARS-CoV-1 and SARS-CoV-2, and a PRD-0038 S protomer can be superimposed with root-mean-square deviation values of 4.9 and 7.2 Å to SARS-CoV-1 S and SARS-CoV-2 S with which it shares 75% and 72% amino acid sequence identity, respectively (Figure S6). Glycosylation at RBD residue N360, which is present in most sarbecoviruses except SARS-CoV-2 (position N370), has been reported to favor the closed S conformation,[39,40] which could possibly explain the sole observation of closed PRD-0038 S trimers in our cryo-EM dataset. However, glycosylation at this site is also present in SARS-CoV-1, which spontaneously adopts open RBD conformations.[41–43] The closed PRD-0038 S RBD conformation is most similar to the linoleic acid (LA)-bound form of SARS-CoV-2 S previously described[44] (Figures 3D and S6). Indeed, the conformation of the RBD helix containing residues 354–359 (equivalent to SARS-CoV-2 residues 364–369) closely resembles that of the linoleic acid-bound SARS-CoV-2 S (Figure 3D) or that of F371-harboring SARS-CoV-2 Omicron variants.[45–48] This conformation, however, is distinct from that observed in the structure of the isolated PRD-0038 RBD bound to *R. alcyone* ACE2 described above (Figure 3E). No linoleic acid density is resolved in our cryo-EM map, although the RBD pocket that accommodates this ligand is conserved in the PRD-0038 S structure, including residues R399 and Q400 (equivalent to SARS-CoV-2 R408 and Q409 forming electrostatic interactions with the linoleic acid carboxylate). Instead, we found that the Y355 side chain (equivalent to SARS-CoV-2 Y365) partially obstructs the hydrophobic pocket, which would have otherwise been occupied by the linoleic acid hydrocarbon tail (Figure 3F). The PRD-0038 S Y355 side chain rotamer

resembles that of apo SARS-CoV-2 S (PDB: 6VXX [5]) and apo SARS-CoV-1 S (PDB: 5X58 [43]), suggesting that this rotameric configuration is accessible to SARS-CoV-2 Y365 and likely changes to allow linoleic acid binding.[44]

Antigenicity of the PRD-0038 S trimer

To define the antigenic landscape of clade 3 sarbecoviruses, we probed binding of a panel of monoclonal antibodies with broadly neutralizing activity against sarbecoviruses[21,22,45,49,50] and α- and β- coronaviruses[51–54] to prefusion-stabilized PRD-0038 S harboring the HexaPro mutations[55] using an enzyme-linked immunosorbent assay (ELISA) (Figure 3G). We found that S2X259[22] and S2X35[49] (antigenic site II) as well as S2H97[21] (antigenic site V) cross-reacted with PRD-0038 S, whereas S309[56] (antigenic site IV) bound very weakly (Figure 3G). The markedly dampened S309 binding likely results from the $E340_{SARS\text{-}CoV\text{-}2}$/$Q330_{PRD\text{-}0038}$ escape substitution previously identified by DMS of the yeast-displayed SARS-CoV-2 Wuhan-Hu-1 RBD[21] (Figure S7). The S2X324[45] antibody (antigenic site Ib), which neutralizes a broad panel of SARS-CoV-2 variants and resembles LY-COV1404,[57] recognizes the SARS-CoV-2 437–448 loop, which is truncated and remodeled in the PRD-0038 RBD, explaining the lack of binding observed (Figure S7). The S2K146[50] antibody (antigenic site Ia), which contacts an epitope sharing several residues with the ACE2-binding site, bound very weakly to wild-type PRD-0038 S, whereas S2M11[58] (antigenic site Ia) did not bind at all, as a result of extensive RBM (receptor-binding motif) mutations (Figure S7). Nevertheless, we previously showed that S2K146 weakly neutralized VSV pseudotyped with BtKY72 S (clade 3) harboring the K482Y/T487W mutations (SARS-CoV-2 numbering 493Y/498W),[50] underscoring the possible usefulness of this antibody if such mutations arose in related clade 3 sarbecoviruses.

The stem helix-targeting S2P6[52] antibody and the RAY53[51] antibody (recognizing the fusion machinery apex) cross-reacted as efficiently with PRD-0038 S as they did with SARS-CoV-2 S, whereas the fusion peptide-directed 76E1 antibody did not, possibly as a result of the $F823_{SARS\text{-}CoV\text{-}2}Y806_{PRD\text{-}0038}$ epitope mutation (which is shared with other clade 3 sarbecoviruses) along with the presence of the $F800P_{PRD\text{-}0038}$ HexaPro stabilizing mutation[54] (Figures 3G and S7).

Consistent with the ELISA data, we found that PRD-0038 K482Y/T487W S VSV pseudovirus was neutralized in a concentration-dependent manner by S2X259, S2X35, and more weakly by 76E1, and the activity of the latter antibody is likely explained by the absence of the $F800P_{PRD\text{-}0038}$ HexaPro stabilizing mutation in our pseudovirus construct (Figures 3G and 3H). Collectively, these data show that monoclonal antibodies targeting RBD antigenic sites or fusion machinery epitopes that are conserved across sarbecoviruses or α- and β- coronaviruses, respectively, retain neutralizing activity against PRD-0038 and are possible candidates for pandemic preparedness.

Immunogenicity of the PRD-0038 S trimer

To better understand the immunogenicity of clade 3 sarbecoviruses and the impact of their possible inclusion in next-generation vaccine candidates, we immunized groups of six mice with three 1 μg doses of either PRD-0038 S or SARS-CoV-2 S (Figure 4A), both stabilized in the prefusion conformation using the HexaPro mutations.[55] Serum-neutralizing activity, expressed as half-maximum inhibition dilution (ID_{50}), was analyzed 2 weeks post dose 3 using VSV particles pseudotyped with clade 1a (SARS-CoV-1), clade 1b (SARS-CoV-2/G614, BA.2, BA.5, RaTG13) or clade 3 (PRD-0038 and Khosta-1) S glycoproteins. SARS-CoV-2 S-immunized mice had the strongest serum-neutralizing activity against SARS-CoV-2/G614 VSV S (ID_{50} = 8,730, vaccine-matched), which was reduced against BA.2 S VSV (ID_{50} = 247) and even more so against BA.5 S VSV (ID_{50} = 71) (Figures 4B and S8). RaTG13 S VSV (vaccine-mismatched), however, was neutralized with almost comparable potency (ID_{50} = 7,752) to that against SARS-CoV-2/G614 S VSV (ID_{50} = 8,730), whereas no neutralization of PRD-0038 S VSV and Khosta-1 S VSV clade 3 sarbecoviruses (vaccine-mismatched) was detected except for a subset of animals with very weak neutralization (mouse 1-1, 1-3, 1-5) (Figures 4B and S8). PRD-0038 S-immunized mice had the strongest serum-neutralizing activity against PRD-0038 S VSV (ID_{50} = 3,634, vaccine-matched) and Khosta-1 S VSV (ID_{50} = 863, vaccine-mismatched), whereas we could not detect any neutralization of clade 1a and 1b pseudoviruses tested besides RaTG13 inhibition (ID_{50} = 928) (Figures 4B and S8). Although none of the sera could block SARS-CoV-1 S-mediated entry into target cells in standard experimental conditions, we observed very weak SARS-CoV-1 S VSV neutralization with greater dilution of the pseudovirus stock when using PRD-0038 S- but not SARS-CoV-2 S-elicited sera (Figure S9). These results suggest that this clade 3 S trimer immunogen induced slightly more broadly neutralizing antibody responses than SARS-CoV-2 S against a clade 1a pseudovirus.

Serum binding titers positively correlate with neutralization potency,[49,59] and the RBD is the main target of neutralizing antibodies against vaccine/infection-matched and mismatched viruses.[49,60–62] We analyzed binding of selected vaccine-elicited sera to a panel of yeast-displayed RBDs spanning the known sarbecovirus phylogenetic diversity using two mice immunized with PRD-0038 S and four mice immunized with SARS-CoV-2 S. We selected two mice with greatest (mouse 1-3, 1-5) and two mice with the weakest (mouse 1-4, 1-6) serum-neutralizing activity against our panel of pseudoviruses from the group immunized with SARS-CoV-2 HexaPro S as well as two mice with the greatest SARS-CoV-1 cross-neutralization (mouse 2-3, 2-6) from the group immunized with PRD-0038 HexaPro S (Figures S8 and S9). In line with the serum neutralization data, inclusion of an antigen in the vaccine formulation was associated with strong cross-reactivity with vaccine-matched and related antigens within the same clade among the sera analyzed (Figures 4C and S10). Furthermore, PRD-0038 S immunization elicited greater titers of antibodies cross-reacting with clade 2 and clade 1a RBDs, as well as the RsYN04 RBD that branches independently of the four previously known clades,[63] likely explaining the weak but detectable SARS-CoV-1 neutralization (Figures 4B, 4C, and S9). These data indicate that inclusion of a clade 3 antigen in a vaccine formulation could not only elicit clade 3 serum-neutralizing activity but also enhance cross-reactive (and weakly neutralizing) antibody responses against vaccine-mismatched antigens from distinct clades, which could participate in protection through direct neutralization and Fc-mediated effector functions.[46,64–67]

CellPress
OPEN ACCESS

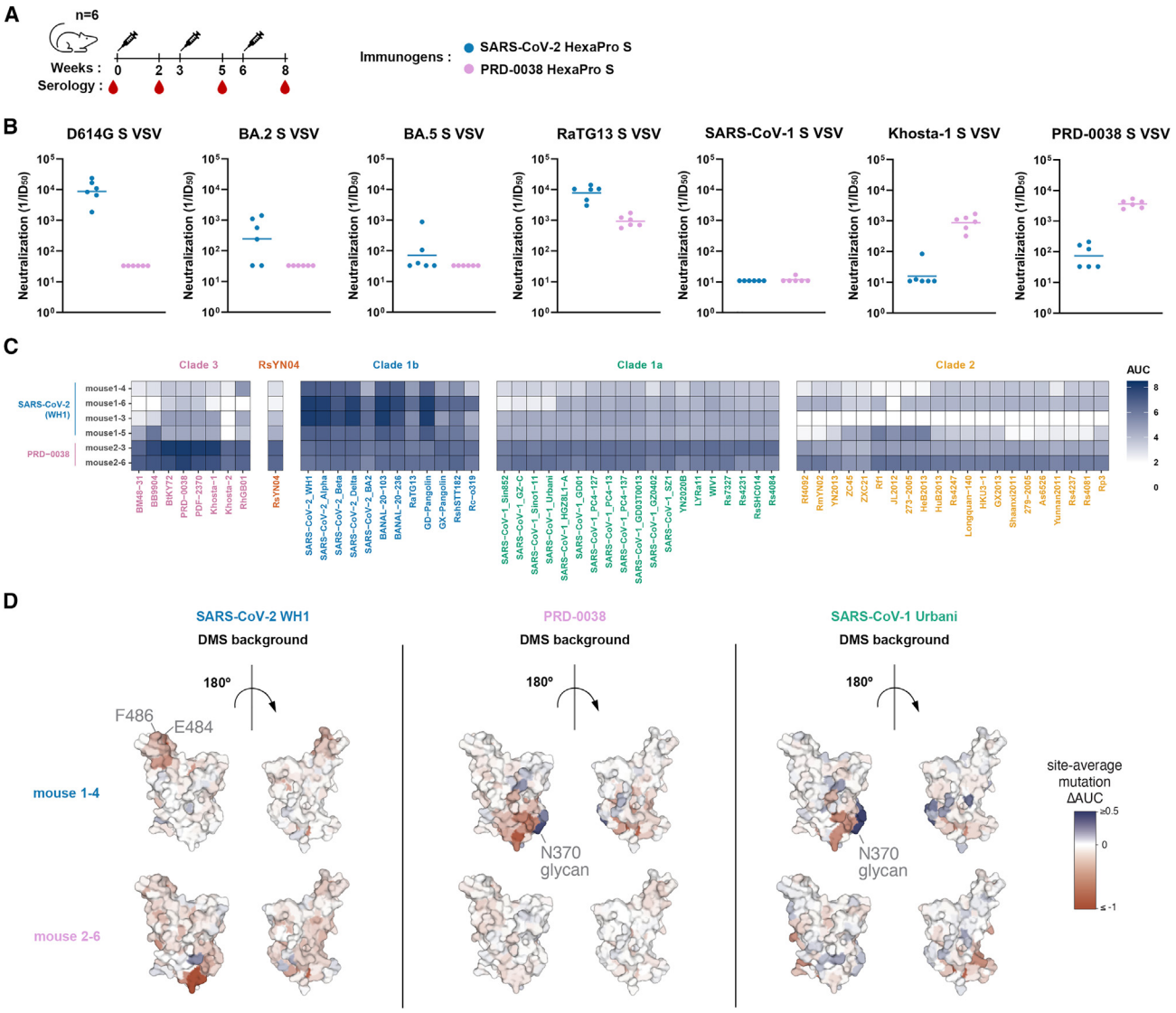

Figure 4. A clade 3 sarbecovirus S trimer elicits broadly reactive antibody responses

(A) Vaccination schedule for the mouse immunogenicity study.

(B) Serum neutralization of VSV pseudotyped with various sarbecovirus S glycoproteins. Bar represents the geometric mean of each group.

(C) Sarbecovirus breadth of serum binding to a pan-sarbecovirus library of yeast-displayed RBDs using a high-throughput FACS-seq assay. The strength of binding is represented as a heat map obtained by plotting the area under the curve (AUC) from titration of various serum dilutions. All the binding curves can be accessed at https://github.com/tstarrlab/SARSr-CoV_MAP_PRD0038-vaccine/blob/main/results/summary/compute_AUC.md#plot-all-curves.

(D) Epitope targeting of serum antibodies. For two representative sera (mouse 1-4, vaccinated with SARS-CoV-2 HexaPro S, and mouse 2-6, vaccinated with PRD-0038 HexaPro S), we determined the dominant antibody epitopes via DMS using vaccine-matched and mismatched RBD backgrounds. The average effect of mutations at each site is mapped to the SARS-CoV-2 structure, where blue and red indicate positions where mutations increase or decrease serum binding, respectively. See Figure S11 for all DMS profiles.

To understand the molecular basis for variation in breadth of serum cross-reactivity across mice and vaccine regimen, we mapped the dominant epitope specificities in these six sera using yeast-displayed DMS libraries in the vaccine-matched SARS-CoV-2 Wuhan-Hu-1 and PRD-0038 RBDs as well as in the vaccine-mismatched SARS-CoV-2 Omicron BA.2 and SARS-CoV-1 Urbani RBDs (Figures 4D and S11). SARS-CoV-2 S-elicited polyclonal serum antibodies predominantly targeted the SARS-CoV-2 Wuhan-Hu-1 RBD region comprising residues 484–490, consistent with the strong antigenic pressure on this position that drove early variant evolution at residue E484 during the COVID-19 pandemic.[68–70] These residues are highly variable among sarbecoviruses, consistent with the weaker cross-reactive breadth seen in these sera. By contrast, PRD-0038 S-elicited polyclonal serum antibodies showed no dominant targeting of specific PRD-0038 RBD antigenic sites, which could indicate a more balanced binding antibody response that would be less susceptible to single amino acid mutations. Epitope

mapping to vaccine-mismatched RBDs revealed that PRD-0038 and SARS-CoV-2 S-elicited sera contained antibodies targeting antigenic sites II, IV, and V,[21,49] which are typically recognized by subdominant broadly-reactive and neutralizing antibodies[21,22,56,71,72] (Figure S11). However, DMS using vaccine-mismatched RBD strains also revealed the presence of antibodies in SARS-CoV-2 S-elicited sera that target suboptimal sites for sarbecovirus breadth. For example, we observed strong antibody responses to the N370 glycan hole (resulting from mutations of this glycosylation sequon in our DMS experiments) for two of the four SARS-CoV-2-immunized mice analyzed. Antibody responses targeting this site are elicited as a result of the absence of this oligosaccharide in the SARS-CoV-2 RBD immunogen but its presence in all other sarbecovirus RBDs. Restoration of the N370 glycan in SARS-CoV-2 vaccines could therefore possibly limit these off-target responses by reducing the elicitation of antibodies to this strain-specific epitope. In conclusion, the DMS data indicate that PRD-0038 S-elicited serum antibodies analyzed here target a broader spectrum of antigenic sites present on vaccine-matched and mismatched RBDs than SARS-CoV-2 S-elicited antibodies, providing a molecular basis for enhanced cross-reactivity (Figures 4D and S11).

DISCUSSION

Coronavirus S glycoproteins are evolutionary hotspots and can acquire amino acid substitutions, insertions, deletions, or even recombine distinct domains.[73] These mutational changes can alter host receptor tropism,[74] binding affinity,[38,75,76] entry route,[46,77,78] and immune evasion.[36,37,75,79–81] Most mutations occur within the RBD, which engage the host receptor and account for most of the neutralizing activity against vaccine/infection-matched and mismatched sarbecoviruses.[49,60–62]

Spillover is a complex process involving multiple factors such as receptor recognition, proteolytic S activation, immune antagonism, and contact opportunity. To examine potential spillover pathways of clade 3 sarbecoviruses, we evaluated binding of PRD-0038 RBD mutants to a panel of *Rhinolophus* bat ACE2 orthologs. Although human ACE2 cannot serve as entry receptor for wild-type PRD-0038 S (or the closely related BtKY72 S[29]), introduction of a single amino acid RBD mutation (T487W) enabled binding and S-mediated entry into cells expressing human ACE2. Moreover, this point mutation broadened host receptor tropism by enabling utilization of the geographically relevant *R. landeri* and *R. ferrumequinum* ACE2 receptors without compromising binding to *R. alcyone*, *R. sinicus*, and *R. affinis* ACE2 alleles. Although the T487W RBD mutation requires 3 nucleotide substitutions, these findings point to a possible spillover pathway in which a single amino acid change expands host receptor tropism markedly. Indeed, acquisition of *R. landeri*, *R. ferrumequinum* (allele FJ598617.1), and human ACE2 tropism would allow PRD-0038 (and likely BtKY72 and related clade 3 viruses) to expand the geographic range of host reservoirs that can be infected and, in turn, the likelihood of zoonotic transmission. Broadly neutralizing antibodies with activity against sarbecoviruses (RBD-directed) and beyond (fusion machinery-directed) inhibited PRD-0038 S-mediated entry into cells and could be stockpiled as possible countermeasures for pandemic preparedness.

We observed that three immunizations with a clade 1b or with a clade 3 sarbecovirus S trimer predominantly elicited vaccine-matched serum-neutralizing antibody responses. We note that our neutralization data of clade 1b pseudoviruses underscore the distinction between antigenic and genetic distance: although RaTG13 harbors a greater number of RBD mutations than Omicron BA.2 or BA.5, neutralizing activity was higher against RaTG13 than against these SARS-CoV-2 variants, which accumulated mutations to erode neutralizing antibody titers.[82,83] Compared with SARS-CoV-2 S, we found that PRD-0038 S-elicited polyclonal serum antibodies were more broadly reactive with vaccine-mismatched antigens, including clades 1a and 2 RBDs, which likely account for the weak but detectable cross-neutralization of SARS-CoV-1 with sera from mice immunized with PRD-0038 S but not with SARS-CoV-2 S. However, we also note that sera from three SARS-CoV-2 S-immunized mice had weak but detectable neutralization against clade 3 sarbecoviruses, whereas none of the PRD-0038 S-elicited sera could neutralize the SARS-CoV-2 S pseudoviruses tested. As non- or weakly neutralizing monoclonal and polyclonal antibodies have been shown to participate in protection against SARS-CoV-2 challenge in small animal models through Fc-mediated effector functions,[46,64–67] our findings motivate the inclusion of clade 3 and other divergent RBDs in updated multi-antigen sarbecovirus vaccine formulations.[84–87] This would allow the elicitation of potent clade 3 neutralizing antibodies and cross-clade binding (and possibly neutralizing) antibodies with maximal breadth to achieve optimal protection against continuously evolving SARS-CoV-2 variants and sarbecoviruses found in wildlife.

Limitations of the study

The analysis of cross-reactivity of vaccine-elicited serum antibodies is based on a small number of animals. Furthermore, there is currently no known animal challenge model for clade 3 sarbecoviruses, and we were therefore not able to evaluate the contribution of the broadly reactive antibody responses elicited upon PRD-0038 S vaccination to *in vivo* protection.

STAR★METHODS

Detailed methods are provided in the online version of this paper and include the following:

- KEY RESOURCES TABLE
- RESOURCE AVAILABILITY
  - Lead contact
  - Materials availability
  - Data and code availability
- EXPERIMENTAL MODEL AND STUDY PARTICIPANT DETAILS
  - Cell lines
  - *In vivo* animal studies
- METHOD DETAILS
  - Production of recombinant PRD-0038 RBDs
  - Production of recombinant ACE2 ectodomains
  - Production of recombinant PRD-0038 PentaPro S, HexaPro S, and SARS-CoV-2 HexaPro S
  - Production of PRD-0038 wild-type RBD- Natively Dimerized R. alcyone Complex

- Binding analysis using biolayer interferometry (BLI)
- Production of VSV pseudoviruses
- Cell entry assays comparing wildtype and mutant PRD-0038 S VSV pseudoviruses
- Cell entry assay for PRD-0038 S VSV with distinct *Rhinolophus* ACE2s
- Cryo-EM sample preparation and data collection
- Cryo-EM data processing, model building and refinement
- Monoclonal antibody ELISAs
- Deep mutational scanning for mutational effects on ACE2 binding
- Immunogenicity
- Neutralization assays
- Breadth- and epitope-mapping of vaccine sera via deep mutational scanning

- QUANTIFICATION AND STATISTICAL ANALYSIS

SUPPLEMENTAL INFORMATION

Supplemental information can be found online at https://doi.org/10.1016/j.chom.2023.10.018.

ACKNOWLEDGMENTS

This study was supported by the National Institute of Allergy and Infectious Diseases (F31AI174573-01 to S.K.Z., K99AI166250 to T.N.S., P01AI167966 to N.P.K, T.N.S., and D.V., and DP1AI158186 and 75N93022C00036 to D.V.), the National Institute of General Medical Sciences (T32GM008268-32 to S.K.Z.), a Pew Biomedical Scholars Award (D.V.), an Investigators in the Pathogenesis of Infectious Disease Awards from the Burroughs Wellcome Fund (D.V.), a Dale F. Frey Award for Breakthrough Scientists from the Damon Runyon Cancer Research Foundation (T.N.S.), the University of Washington Arnold and Mabel Beckman Cryo-EM Center, and the National Institute of Health grant S10OD032290 (to D.V.). D.V. is an investigator of the Howard Hughes Medical Institute and the Hans Neurath Endowed Chair in Biochemistry at the University of Washington. We thank the High-Throughput Genomics Shared Resource at the University of Utah Huntsman Cancer Institute supported by NCI/NIH (P30CA042014), the Flow Cytometry Core Facility at the University of Utah Health Sciences Campus supported by NIH (S10OD026959 and 5P30CA042014-24), the University of Utah Center for High Performance Computing, supported by NIH (1S10OD021644-01A1), and the Fred Hutchinson Cancer Center Genomics core facility for experimental support.

AUTHOR CONTRIBUTIONS

J.L., S.K.Z., T.S., and D.V. designed the experiments. J.L., S.K.Z., and C.S. recombinantly expressed and purified glycoproteins. J.L. and S.K.Z. performed binding assays. J.L. carried out pseudovirus entry assays. J.L., S.K.Z., J.Q., and Y.-J.P. carried out cryo-EM specimen preparation, data collection, and processing of PRD-0038 S. J.L., S.K.Z., and Y.-J.P. carried out cryo-EM specimen preparation, data collection, and processing of the PRD-0038 RBD bound to ACE2. J.L., Y.-J.P., and D.V. built and refined atomic models. E.M.L. and C.T. performed mouse immunizations and blood draws. A.L.T. and T.N.S. carried out DMS experiments. D.C. contributed unique reagents. J.L. and D.V. analyzed the data and wrote the manuscript with input from all authors. N.P.K., T.N.S., and D.V. supervised the project.

DECLARATION OF INTERESTS

N.P.K. and D.V. are named as inventors on patents for coronavirus nanoparticle vaccines filed by the University of Washington. N.P.K. is a co-founder, shareholder, paid consultant, and chair of the scientific advisory board of Icosavax, Inc. and has received an unrelated sponsored research agreement from Pfizer. D.C. is an employee of Vir Biotechnology and may hold shares in Vir Biotechnology. T.N.S. consults for Apriori Bio on DMS. The lab of T.N.S. has received sponsored research agreements unrelated to the present work from Vir Biotechnology and Aerium Therapeutics, Inc. T.N.S. may receive a share of intellectual property revenue as inventor on a Fred Hutchinson Cancer Center-optioned patent related to stabilization of SARS-CoV-2 RBDs. The remaining authors declare that the research was conducted in the absence of any commercial or financial relationships that could be construed as a potential conflict of interest.

Received: September 5, 2023
Revised: October 12, 2023
Accepted: October 24, 2023
Published: December 13, 2023

REFERENCES

1. Drosten, C., Günther, S., Preiser, W., van der Werf, S., Brodt, H.R., Becker, S., Rabenau, H., Panning, M., Kolesnikova, L., Fouchier, R.A., et al. (2003). Identification of a novel coronavirus in patients with severe acute respiratory syndrome. N. Engl. J. Med. *348*, 1967–1976.
2. Ksiazek, T.G., Erdman, D., Goldsmith, C.S., Zaki, S.R., Peret, T., Emery, S., Tong, S., Urbani, C., Comer, J.A., Lim, W., et al. (2003). A novel coronavirus associated with severe acute respiratory syndrome. N. Engl. J. Med. *348*, 1953–1966.
3. Zhou, P., Yang, X.L., Wang, X.G., Hu, B., Zhang, L., Zhang, W., Si, H.R., Zhu, Y., Li, B., Huang, C.L., et al. (2020). A pneumonia outbreak associated with a new coronavirus of probable bat origin. Nature *579*, 270–273. https://doi.org/10.1038/s41586-020-2012-7.
4. Zhu, N., Zhang, D., Wang, W., Li, X., Yang, B., Song, J., Zhao, X., Huang, B., Shi, W., Lu, R., et al. (2020). A novel coronavirus from patients with pneumonia in China, 2019. N. Engl. J. Med. *382*, 727–733. https://doi.org/10.1056/NEJMoa2001017.
5. Walls, A.C., Park, Y.J., Tortorici, M.A., Wall, A., McGuire, A.T., and Veesler, D. (2020). Structure, function, and antigenicity of the SARS-CoV-2 spike glycoprotein. Cell *181*, 281.
6. Letko, M., Marzi, A., and Munster, V. (2020). Functional assessment of cell entry and receptor usage for SARS-CoV-2 and other lineage B betacoronaviruses. Nat. Microbiol. *5*, 562–569.
7. Hoffmann, M., Kleine-Weber, H., Schroeder, S., Krüger, N., Herrler, T., Erichsen, S., Schiergens, T.S., Herrler, G., Wu, N.H., Nitsche, A., et al. (2020). SARS-CoV-2 cell entry depends on ACE2 and TMPRSS2 and is blocked by a clinically proven protease inhibitor. Cell *181*, 271–280.e8.
8. Li, W., Moore, M.J., Vasilieva, N., Sui, J., Wong, S.K., Berne, M.A., Somasundaran, M., Sullivan, J.L., Luzuriaga, K., Greenough, T.C., et al. (2003). Angiotensin-converting enzyme 2 is a functional receptor for the SARS coronavirus. Nature *426*, 450–454.
9. Evans, T.S., Tan, C.W., Aung, O., Phyu, S., Lin, H., Coffey, L.L., Toe, A.T., Aung, P., Aung, T.H., Aung, N.T., et al. (2023). Exposure to diverse sarbecoviruses indicates frequent zoonotic spillover in human communities interacting with wildlife. Int. J. Infect. Dis. *131*, 57–64. https://doi.org/10.1016/j.ijid.2023.02.015.
10. Wang, N., Li, S.Y., Yang, X.L., Huang, H.M., Zhang, Y.J., Guo, H., Luo, C.M., Miller, M., Zhu, G., Chmura, A.A., et al. (2018). Serological evidence of bat SARS-related coronavirus infection in humans, China. Virol. Sin. *33*, 104–107.
11. Wacharapluesadee, S., Tan, C.W., Maneeorn, P., Duengkae, P., Zhu, F., Joyjinda, Y., Kaewpom, T., Chia, W.N., Ampoot, W., Lim, B.L., et al. (2021). Evidence for SARS-CoV-2 related coronaviruses circulating in bats and pangolins in Southeast Asia. Nat. Commun. *12*. https://doi.org/10.1038/s41467-021-21240-1.
12. Temmam, S., Vongphayloth, K., Baquero, E., Munier, S., Bonomi, M., Regnault, B., Douangboubpha, B., Karami, Y., Chrétien, D., Sanamxay, D., et al. (2022). Bat coronaviruses related to SARS-CoV-2 and infectious for human cells. Nature *604*, 330–336. https://doi.org/10.1038/s41586-022-04532-4.

13. Lam, T.T., Jia, N., Zhang, Y.W., Shum, M.H., Jiang, J.F., Zhu, H.C., Tong, Y.G., Shi, Y.X., Ni, X.B., Liao, Y.S., et al. (2020). Identifying SARS-CoV-2 related coronaviruses in Malayan pangolins. Nature *583*, 282–285. https://doi.org/10.1038/s41586-020-2169-0.

14. Ge, X.Y., Li, J.L., Yang, X.L., Chmura, A.A., Zhu, G., Epstein, J.H., Mazet, J.K., Hu, B., Zhang, W., Peng, C., et al. (2013). Isolation and characterization of a bat SARS-like coronavirus that uses the ACE2 receptor. Nature *503*, 535–538.

15. Hu, B., Zeng, L.P., Yang, X.L., Ge, X.Y., Zhang, W., Li, B., Xie, J.Z., Shen, X.R., Zhang, Y.Z., Wang, N., et al. (2017). Discovery of a rich gene pool of bat SARS-related coronaviruses provides new insights into the origin of SARS coronavirus. PLoS Pathog. *13*, e1006698.

16. Yang, X.L., Hu, B., Wang, B., Wang, M.N., Zhang, Q., Zhang, W., Wu, L.J., Ge, X.Y., Zhang, Y.Z., Daszak, P., et al. (2015). Isolation and characterization of a novel bat coronavirus closely related to the direct progenitor of severe acute respiratory syndrome coronavirus. J. Virol. *90*, 3253–3256.

17. Wrobel, A.G., Benton, D.J., Xu, P., Calder, L.J., Borg, A., Roustan, C., Martin, S.R., Rosenthal, P.B., Skehel, J.J., and Gamblin, S.J. (2021). Structure and binding properties of Pangolin-CoV spike glycoprotein inform the evolution of SARS-CoV-2. Nat. Commun. *12*, 837.

18. Niu, S., Wang, J., Bai, B., Wu, L., Zheng, A., Chen, Q., Du, P., Han, P., Zhang, Y., Jia, Y., et al. (2022). Molecular basis of cross-species ACE2 interactions with SARS-CoV-2-like viruses of pangolin origin. EMBO J. *41*, e109962.

19. Menachery, V.D., Yount, B.L., Sims, A.C., Debbink, K., Agnihothram, S.S., Gralinski, L.E., Graham, R.L., Scobey, T., Plante, J.A., Royal, S.R., et al. (2016). SARS-like WIV1-CoV poised for human emergence. Proc. Natl. Acad. Sci. USA *113*, 3048–3053.

20. Menachery, V.D., Yount, B.L., Debbink, K., Agnihothram, S., Gralinski, L.E., Plante, J.A., Graham, R.L., Scobey, T., Ge, X.Y., Donaldson, E.F., et al. (2015). A SARS-like cluster of circulating bat coronaviruses shows potential for human emergence. Nat. Med. *21*, 1508–1513.

21. Starr, T.N., Czudnochowski, N., Liu, Z., Zatta, F., Park, Y.J., Addetia, A., Pinto, D., Beltramello, M., Hernandez, P., Greaney, A.J., et al. (2021). SARS-CoV-2 RBD antibodies that maximize breadth and resistance to escape. Nature *597*, 97–102. https://doi.org/10.1038/s41586-021-03807-6.

22. Tortorici, M.A., Czudnochowski, N., Starr, T.N., Marzi, R., Walls, A.C., Zatta, F., Bowen, J.E., Jaconi, S., Di Iulio, J., Wang, Z., et al. (2021). Broad sarbecovirus neutralization by a human monoclonal antibody. Nature *597*, 103–108. https://doi.org/10.1038/s41586-021-03817-4.

23. Tong, S., Conrardy, C., Ruone, S., Kuzmin, I.V., Guo, X., Tao, Y., Niezgoda, M., Haynes, L., Agwanda, B., Breiman, R.F., et al. (2009). Detection of novel SARS-like and other coronaviruses in bats from Kenya. Emerg. Infect. Dis. *15*, 482–485.

24. Tao, Y., and Tong, S. (2019). Complete genome sequence of a severe acute respiratory syndrome-related coronavirus from Kenyan bats. Microbiol. Resour. Announc. *8*. https://doi.org/10.1128/MRA.00548-19.

25. Wells, H.L., Letko, M., Lasso, G., Ssebide, B., Nziza, J., Byarugaba, D.K., Navarrete-Macias, I., Liang, E., Cranfield, M., Han, B.A., et al. (2021). The evolutionary history of ACE2 usage within the coronavirus subgenus Sarbecovirus. Virus Evol. *7*, veab007.

26. Drexler, J.F., Gloza-Rausch, F., Glende, J., Corman, V.M., Muth, D., Goettsche, M., Seebens, A., Niedrig, M., Pfefferle, S., Yordanov, S., et al. (2010). Genomic characterization of severe acute respiratory syndrome-related coronavirus in European bats and classification of coronaviruses based on partial RNA-dependent RNA polymerase gene sequences. J. Virol. *84*, 11336–11349.

27. Crook, J.M., Murphy, I., Carter, D.P., Pullan, S.T., Carroll, M., Vipond, R., Cunningham, A.A., and Bell, D. (2021). Metagenomic identification of a new sarbecovirus from horseshoe bats in Europe. Sci. Rep. *11*, 14723.

28. Alkhovsky, S., Lenshin, S., Romashin, A., Vishnevskaya, T., Vyshemirsky, O., Bulycheva, Y., Lvov, D., and Gitelman, A. (2022). SARS-like coronaviruses in horseshoe bats (Rhinolophus spp.) in Russia, 2020. Viruses *14*. https://doi.org/10.3390/v14010113.

29. Starr, T.N., Zepeda, S.K., Walls, A.C., Greaney, A.J., Alkhovsky, S., Veesler, D., and Bloom, J.D. (2022). ACE2 binding is an ancestral and evolvable trait of sarbecoviruses. Nature *603*, 913–918.

30. Seifert, S.N., Bai, S., Fawcett, S., Norton, E.B., Zwezdaryk, K.J., Robinson, J., Gunn, B., and Letko, M.C. (2022). An ACE2-dependent Sarbecovirus in Russian bats is resistant to SARS-CoV-2 vaccines. PLoS Pathog. *18*, e1010828. https://doi.org/10.1371/journal.ppat.1010828.

31. Guo, H., Hu, B.J., Yang, X.L., Zeng, L.P., Li, B., Ouyang, S., and Shi, Z.L. (2020). Evolutionary arms race between virus and host drives genetic diversity in bat severe acute respiratory syndrome-related coronavirus spike genes. J. Virol. *94*. https://doi.org/10.1128/JVI.00902-20.

32. Roelle, S.M., Shukla, N., Pham, A.T., Bruchez, A.M., and Matreyek, K.A. (2022). Expanded ACE2 dependencies of diverse SARS-like coronavirus receptor binding domains. PLoS Biol. *20*, e3001738.

33. Lan, J., Ge, J., Yu, J., Shan, S., Zhou, H., Fan, S., Zhang, Q., Shi, X., Wang, Q., Zhang, L., et al. (2020). Structure of the SARS-CoV-2 spike receptor-binding domain bound to the ACE2 receptor. Nature *581*, 215–220. https://doi.org/10.1038/s41586-020-2180-5.

34. Li, F., Li, W., Farzan, M., and Harrison, S.C. (2005). Structure of SARS coronavirus spike receptor-binding domain complexed with receptor. Science *309*, 1864–1868.

35. Leist, S.R., Dinnon, K.H., 3rd, Schäfer, A., Tse, L.V., Okuda, K., Hou, Y.J., West, A., Edwards, C.E., Sanders, W., Fritch, E.J., et al. (2020). A mouse-adapted SARS-CoV-2 induces acute lung injury and mortality in standard laboratory mice. Cell *183*, 1070–1085.e12.

36. Cameroni, E., Bowen, J.E., Rosen, L.E., Saliba, C., Zepeda, S.K., Culap, K., Pinto, D., VanBlargan, L.A., De Marco, A., di Iulio, J., et al. (2021). Broadly neutralizing antibodies overcome SARS-CoV-2 Omicron antigenic shift. Nature *602*, 664–670. https://doi.org/10.1038/d41586-021-03825-4.

37. McCallum, M., Czudnochowski, N., Rosen, L.E., Zepeda, S.K., Bowen, J.E., Walls, A.C., Hauser, K., Joshi, A., Stewart, C., Dillen, J.R., et al. (2022). Structural Basis of SARS-CoV-2 Omicron Immune Evasion and Receptor Engagement. Science, eabn8652.

38. Starr, T.N., Greaney, A.J., Stewart, C.M., Walls, A.C., Hannon, W.W., Veesler, D., and Bloom, J.D. (2022). Deep mutational scans for ACE2 binding, RBD expression, and antibody escape in the SARS-CoV-2 Omicron BA.1 and BA.2 receptor-binding domains. PLoS Pathog. *18*, e1010951.

39. Harbison, A.M., Fogarty, C.A., Phung, T.K., Satheesan, A., Schulz, B.L., and Fadda, E. (2022). Fine-tuning the spike: role of the nature and topology of the glycan shield in the structure and dynamics of the SARS-CoV-2 S. Chem. Chem. Sci. *13*, 386–395.

40. Zhang, S., Liang, Q., He, X., Zhao, C., Ren, W., Yang, Z., Wang, Z., Ding, Q., Deng, H., Wang, T., et al. (2022). Loss of Spike N370 glycosylation as an important evolutionary event for the enhanced infectivity of SARS-CoV-2. Cell Res. *32*, 315–318.

41. Walls, A.C., Xiong, X., Park, Y.J., Tortorici, M.A., Snijder, J., Quispe, J., Cameroni, E., Gopal, R., Dai, M., Lanzavecchia, A., et al. (2019). Unexpected receptor functional mimicry elucidates activation of coronavirus fusion. Cell *176*, 1026–1039.e15.

42. Kirchdoerfer, R.N., Wang, N., Pallesen, J., Wrapp, D., Turner, H.L., Cottrell, C.A., Corbett, K.S., Graham, B.S., McLellan, J.S., and Ward, A.B. (2018). Stabilized coronavirus spikes are resistant to conformational changes induced by receptor recognition or proteolysis. Sci. Rep. *8*, 15701.

43. Yuan, Y., Cao, D., Zhang, Y., Ma, J., Qi, J., Wang, Q., Lu, G., Wu, Y., Yan, J., Shi, Y., et al. (2017). Cryo-EM structures of MERS-CoV and SARS-CoV spike glycoproteins reveal the dynamic receptor binding domains. Nat. Commun. *8*, 15092.

44. Toelzer, C., Gupta, K., Yadav, S.K.N., Borucu, U., Davidson, A.D., Kavanagh Williamson, M., Shoemark, D.K., Garzoni, F., Staufer, O., Milligan, R., et al. (2020). Free fatty acid binding pocket in the locked structure of SARS-CoV-2 spike protein. Science *370*, 725–730.

45. Park, Y.-J., Pinto, D., Walls, A.C., Liu, Z., De Marco, A., Benigni, F., Zatta, F., Silacci-Fregni, C., Bassi, J., Sprouse, K.R., et al. (2022). Imprinted antibody responses against SARS-CoV-2 Omicron sublineages. Science, eadc9127.

46. Addetia, A., Piccoli, L., Case, J.B., Park, Y.J., Beltramello, M., Guarino, B., Dang, H., Pinto, D., Scheaffer, S.M., Sprouse, K., et al. (2023). Therapeutic and vaccine-induced cross-reactive antibodies with effector function against emerging Omicron variants. Preprint at bioRxiv. https://doi.org/10.1101/2023.01.17.523798.

47. Stalls, V., Lindenberger, J., Gobeil, S.M.-C., Henderson, R., Parks, R., Barr, M., Deyton, M., Martin, M., Janowska, K., Huang, X., et al. (2022). Cryo-EM structures of SARS-CoV-2 Omicron BA.2 spike. Cell Rep. *39*, 111009.

48. Cao, Y., Yisimayi, A., Jian, F., Song, W., Xiao, T., Wang, L., Du, S., Wang, J., Li, Q., Chen, X., et al. (2022). BA.2.12.1, BA.4 and BA.5 escape antibodies elicited by Omicron infection. Nature *608*, 593–602.

49. Piccoli, L., Park, Y.J., Tortorici, M.A., Czudnochowski, N., Walls, A.C., Beltramello, M., Silacci-Fregni, C., Pinto, D., Rosen, L.E., Bowen, J.E., et al. (2020). Mapping neutralizing and immunodominant sites on the SARS-CoV-2 spike receptor-binding domain by structure-guided high-resolution serology. Cell *183*, 1024–1042.e21.

50. Park, Y.-J., De Marco, A., Starr, T.N., Liu, Z., Pinto, D., Walls, A.C., Zatta, F., Zepeda, S.K., Bowen, J.E., Sprouse, K.R., et al. (2022). Antibody-mediated broad sarbecovirus neutralization through ACE2 molecular mimicry. Science, eabm8143.

51. Silva, R.P., Huang, Y., Nguyen, A.W., Hsieh, C.L., Olaluwoye, O.S., Kaoud, T.S., Wilen, R.E., Qerqez, A.N., Park, J.G., Khalil, A.M., et al. (2023). Identification of a conserved S2 epitope present on spike proteins from all highly pathogenic coronaviruses. eLife *12*. https://doi.org/10.7554/eLife.83710.

52. Pinto, D., Sauer, M.M., Czudnochowski, N., Low, J.S., Tortorici, M.A., Housley, M.P., Noack, J., Walls, A.C., Bowen, J.E., Guarino, B., et al. (2021). Broad Betacoronavirus neutralization by a stem helix–specific human antibody. Science *373*, 1109–1116. https://doi.org/10.1126/science.abj3321.

53. Sauer, M.M., Tortorici, M.A., Park, Y.J., Walls, A.C., Homad, L., Acton, O.J., Bowen, J.E., Wang, C., Xiong, X., de van der Schueren, W., et al. (2021). Structural basis for broad coronavirus neutralization. Nat. Struct. Mol. Biol. *28*, 478–486.

54. Low, J.S., Jerak, J., Tortorici, M.A., McCallum, M., Pinto, D., Cassotta, A., Foglierini, M., Mele, F., Abdelnabi, R., Weynand, B., et al. (2022). ACE2-binding exposes the SARS-CoV-2 fusion peptide to broadly neutralizing coronavirus antibodies. Science *377*, 735–742.

55. Hsieh, C.L., Goldsmith, J.A., Schaub, J.M., DiVenere, A.M., Kuo, H.C., Javanmardi, K., Le, K.C., Wrapp, D., Lee, A.G., Liu, Y., et al. (2020). Structure-based design of prefusion-stabilized SARS-CoV-2 spikes. Science *369*, 1501–1505. https://doi.org/10.1126/science.abd0826.

56. Pinto, D., Park, Y.J., Beltramello, M., Walls, A.C., Tortorici, M.A., Bianchi, S., Jaconi, S., Culap, K., Zatta, F., De Marco, A., et al. (2020). Cross-neutralization of SARS-CoV-2 by a human monoclonal SARS-CoV antibody. Nature *583*, 290–295.

57. Westendorf, K., Žentelis, S., Wang, L., Foster, D., Vaillancourt, P., Wiggin, M., Lovett, E., van der Lee, R., Hendle, J., Pustilnik, A., et al. (2022). LY-CoV1404 (bebtelovimab) potently neutralizes SARS-CoV-2 variants. Cell Rep. *39*, 110812.

58. Tortorici, M.A., Beltramello, M., Lempp, F.A., Pinto, D., Dang, H.V., Rosen, L.E., McCallum, M., Bowen, J., Minola, A., Jaconi, S., et al. (2020). Ultrapotent human antibodies protect against SARS-CoV-2 challenge via multiple mechanisms. Science *370*, 950–957.

59. Robbiani, D.F., Gaebler, C., Muecksch, F., Lorenzi, J.C.C., Wang, Z., Cho, A., Agudelo, M., Barnes, C.O., Gazumyan, A., Finkin, S., et al. (2020). Convergent antibody responses to SARS-CoV-2 in convalescent individuals. Nature *584*, 437–442. https://doi.org/10.1038/s41586-020-2456-9.

60. Bowen, J.E., Park, Y.J., Stewart, C., Brown, J.T., Sharkey, W.K., Walls, A.C., Joshi, A., Sprouse, K.R., McCallum, M., Tortorici, M.A., et al. (2022). SARS-CoV-2 spike conformation determines plasma neutralizing activity elicited by a wide panel of human vaccines. Sci. Immunol. *7*, eadf1421. https://doi.org/10.1126/sciimmunol.adf1421.

61. Greaney, A.J., Loes, A.N., Gentles, L.E., Crawford, K.H.D., Starr, T.N., Malone, K.D., Chu, H.Y., and Bloom, J.D. (2021). Antibodies elicited by mRNA-1273 vaccination bind more broadly to the receptor binding domain than do those from SARS-CoV-2 infection. Sci. Transl. Med. *13*. https://doi.org/10.1126/scitranslmed.abi9915.

62. Stamatatos, L., Czartoski, J., Wan, Y.H., Homad, L.J., Rubin, V., Glantz, H., Neradilek, M., Seydoux, E., Jennewein, M.F., MacCamy, A.J., et al. (2021). mRNA vaccination boosts cross-variant neutralizing antibodies elicited by SARS-CoV-2 infection. Science *372*, 1413–1418. https://doi.org/10.1126/science.abg9175.

63. Zhou, H., Ji, J., Chen, X., Bi, Y., Li, J., Wang, Q., Hu, T., Song, H., Zhao, R., Chen, Y., et al. (2021). Identification of novel bat coronaviruses sheds light on the evolutionary origins of SARS-CoV-2 and related viruses. Cell *184*, 4380–4391.e14.

64. Schäfer, A., Muecksch, F., Lorenzi, J.C.C., Leist, S.R., Cipolla, M., Bournazos, S., Schmidt, F., Maison, R.M., Gazumyan, A., Martinez, D.R., et al. (2021). Antibody potency, effector function, and combinations in protection and therapy for SARS-CoV-2 infection in vivo. J. Exp. Med. *218*. https://doi.org/10.1084/jem.20201993.

65. Winkler, E.S., Gilchuk, P., Yu, J., Bailey, A.L., Chen, R.E., Chong, Z., Zost, S.J., Jang, H., Huang, Y., Allen, J.D., et al. (2021). Human neutralizing antibodies against SARS-CoV-2 require intact Fc effector functions for optimal therapeutic protection. Cell *184*, 1804–1820.e16.

66. Adams, L.E., Leist, S.R., Dinnon, K.H., 3rd, West, A., Gully, K.L., Anderson, E.J., Loome, J.F., Madden, E.A., Powers, J.M., Schäfer, A., et al. (2023). Fc-mediated pan-sarbecovirus protection after alphavirus vector vaccination. Cell Rep. *42*, 112326.

67. Mackin, S.R., Desai, P., Whitener, B.M., Karl, C.E., Liu, M., Baric, R.S., Edwards, D.K., Chicz, T.M., McNamara, R.P., Alter, G., et al. (2023). Fc-γR-dependent antibody effector functions are required for vaccine-mediated protection against antigen-shifted variants of SARS-CoV-2. Nat. Microbiol. *8*, 569–580.

68. Tegally, H., Wilkinson, E., Giovanetti, M., Iranzadeh, A., Fonseca, V., Giandhari, J., Doolabh, D., Pillay, S., San, E.J., Msomi, N., et al. (2021). Emergence of a SARS-CoV-2 variant of concern with mutations in spike glycoprotein. Nature *592*, 438–443. https://doi.org/10.1038/s41586-021-03402-9.

69. Freitas, A.R.R., Beckedorff, O.A., de Góes Cavalcanti, L.P., Siqueira, A.M., de Castro, D.B., da Costa, C.F., Lemos, D.R.Q., and Barros, E.N.C. (2021). The emergence of novel SARS-CoV-2 variant P.1 in Amazonas (Brazil) was temporally associated with a change in the age and sex profile of COVID-19 mortality: a population based ecological study. The Lancet Regional Health – Americas *1*. https://doi.org/10.1016/j.lana.2021.100021.

70. Fujino, T., Nomoto, H., Kutsuna, S., Ujiie, M., Suzuki, T., Sato, R., Fujimoto, T., Kuroda, M., Wakita, T., and Ohmagari, N. (2021). Novel SARS-CoV-2 variant in travelers from brazil to Japan. Emerg. Infect. Dis. *27*, 1243–1245.

71. Jette, C.A., Cohen, A.A., Gnanapragasam, P.N.P., Muecksch, F., Lee, Y.E., Huey-Tubman, K.E., Schmidt, F., Hatziioannou, T., Bieniasz, P.D., Nussenzweig, M.C., et al. (2021). Broad cross-reactivity across sarbecoviruses exhibited by a subset of COVID-19 donor-derived neutralizing antibodies. Cell Rep. *36*, 109760.

72. Martinez, D.R., Schäfer, A., Gobeil, S., Li, D., De la Cruz, G., Parks, R., Lu, X., Barr, M., Stalls, V., Janowska, K., et al. (2021). A broadly cross-reactive antibody neutralizes and protects against sarbecovirus challenge in mice. Sci. Transl. Med. *14*, eabj7125.

73. (2022). SARS-CoV-2 evolution, post-Omicron. Virological. https://virological.org/t/sars-cov-2-evolution-post-omicron/911.

74. Xiong, Q., Cao, L., Ma, C., Tortorici, M.A., Liu, C., Si, J., Liu, P., Gu, M., Walls, A.C., Wang, C., et al. (2022). Close relatives of MERS-CoV in bats use ACE2 as their functional receptors. Nature *612*, 748–757.

75. Bowen, J.E., Addetia, A., Dang, H.V., Stewart, C., Brown, J.T., Sharkey, W.K., Sprouse, K.R., Walls, A.C., Mazzitelli, I.G., Logue, J.K., et al. (2022). Omicron spike function and neutralizing activity elicited by a comprehensive panel of vaccines. Science *377*, 890–894.

76. Starr, T.N., Greaney, A.J., Hilton, S.K., Ellis, D., Crawford, K.H.D., Dingens, A.S., Navarro, M.J., Bowen, J.E., Tortorici, M.A., Walls, A.C., et al. (2020). Deep mutational scanning of SARS-CoV-2 receptor binding domain reveals constraints on folding and ACE2 binding. Cell *182*, 1295–1310.e20.

77. Meng, B., Abdullahi, A., Ferreira, I.A.T.M., Goonawardane, N., Saito, A., Kimura, I., Yamasoba, D., Gerber, P.P., Fatihi, S., Rathore, S., et al. (2022). Altered TMPRSS2 usage by SARS-CoV-2 Omicron impacts infectivity and fusogenicity. Nature *603*, 706–714.

78. Willett, B.J., Grove, J., MacLean, O.A., Wilkie, C., De Lorenzo, G., Furnon, W., Cantoni, D., Scott, S., Logan, N., Ashraf, S., et al. (2022). SARS-CoV-2 Omicron is an immune escape variant with an altered cell entry pathway. Nat. Microbiol. *7*, 1161–1179.

79. Starr, T.N., Greaney, A.J., Hannon, W.W., Loes, A.N., Hauser, K., Dillen, J.R., Ferri, E., Farrell, A.G., Dadonaite, B., McCallum, M., et al. (2022). Shifting mutational constraints in the SARS-CoV-2 receptor-binding domain during viral evolution. Science *377*, 420–424. https://doi.org/10.1126/science.abo7896.

80. McCallum, M., De Marco, A., Lempp, F.A., Tortorici, M.A., Pinto, D., Walls, A.C., Beltramello, M., Chen, A., Liu, Z., Zatta, F., et al. (2021). N-terminal domain antigenic mapping reveals a site of vulnerability for SARS-CoV-2. Cell *184*, 2332–2347.e16.

81. McCallum, M., Bassi, J., De Marco, A., Chen, A., Walls, A.C., Di Iulio, J., Tortorici, M.A., Navarro, M.J., Silacci-Fregni, C., Saliba, C., et al. (2021). SARS-CoV-2 immune evasion by the B.1.427/B.1.429 variant of concern. Science *373*, 648–654. https://doi.org/10.1126/science.abi7994.

82. Cao, Y., Jian, F., Wang, J., Yu, Y., Song, W., Yisimayi, A., Wang, J., An, R., Chen, X., Zhang, N., et al. (2023). Imprinted SARS-CoV-2 humoral immunity induces convergent Omicron RBD evolution. Nature *614*, 521–529.

83. Tan, C.W., Chia, W.N., Zhu, F., Young, B.E., Chantasrisawad, N., Hwa, S.H., Yeoh, A.Y.-Y., Lim, B.L., Yap, W.C., Pada, S.K.M.S., et al. (2022). SARS-CoV-2 Omicron variant emerged under immune selection. Nat. Microbiol. *7*, 1756–1761.

84. Walls, A.C., Miranda, M.C., Schäfer, A., Pham, M.N., Greaney, A., Arunachalam, P.S., Navarro, M.J., Tortorici, M.A., Rogers, K., O'Connor, M.A., et al. (2021). Elicitation of broadly protective sarbecovirus immunity by receptor-binding domain nanoparticle vaccines. Cell *184*, 5432–5447.e16. https://doi.org/10.1016/j.cell.2021.09.015.

85. Cohen, A.A., van Doremalen, N., Greaney, A.J., Andersen, H., Sharma, A., Starr, T.N., Keeffe, J.R., Fan, C., Schulz, J.E., Gnanapragasam, P.N.P., et al. (2022). Mosaic RBD nanoparticles protect against challenge by diverse sarbecoviruses in animal models. Science *377*, eabq0839.

86. Cohen, A.A., Gnanapragasam, P.N.P., Lee, Y.E., Hoffman, P.R., Ou, S., Kakutani, L.M., Keeffe, J.R., Wu, H.J., Howarth, M., West, A.P., et al. (2021). Mosaic nanoparticles elicit cross-reactive immune responses to zoonotic coronaviruses in mice. Science *371*, 735–741.

87. Martinez, D.R., Schäfer, A., Leist, S.R., De la Cruz, G., West, A., Atochina-Vasserman, E.N., Lindesmith, L.C., Pardi, N., Parks, R., Barr, M., et al. (2021). Chimeric spike mRNA vaccines protect against Sarbecovirus challenge in mice. Science *373*, 991–998. https://doi.org/10.1126/science.abi4506.

88. Crawford, K.H.D., Eguia, R., Dingens, A.S., Loes, A.N., Malone, K.D., Wolf, C.R., Chu, H.Y., Tortorici, M.A., Veesler, D., Murphy, M., et al. (2020). Protocol and reagents for pseudotyping lentiviral particles with SARS-CoV-2 spike protein for neutralization assays. Viruses *12*. https://doi.org/10.3390/v12050513.

89. Kaname, Y., Tani, H., Kataoka, C., Shiokawa, M., Taguwa, S., Abe, T., Moriishi, K., Kinoshita, T., and Matsuura, Y. (2010). Acquisition of complement resistance through incorporation of CD55/decay-accelerating factor into viral particles bearing baculovirus GP64. J. Virol. *84*, 3210–3219.

90. Snijder, J., Borst, A.J., Dosey, A., Walls, A.C., Burrell, A., Reddy, V.S., Kollman, J.M., and Veesler, D. (2017). Vitrification after multiple rounds of sample application and blotting improves particle density on cryo-electron microscopy grids. J. Struct. Biol. *198*, 38–42.

91. Suloway, C., Pulokas, J., Fellmann, D., Cheng, A., Guerra, F., Quispe, J., Stagg, S., Potter, C.S., and Carragher, B. (2005). Automated molecular microscopy: the new Leginon system. J. Struct. Biol. *151*, 41–60.

92. Tegunov, D., and Cramer, P. (2019). Real-time cryo-electron microscopy data preprocessing with Warp. Nat. Methods *16*, 1146–1152.

93. Punjani, A., Rubinstein, J.L., Fleet, D.J., and Brubaker, M.A. (2017). cryoSPARC: algorithms for rapid unsupervised cryo-EM structure determination. Nat. Methods *14*, 290–296.

94. Zivanov, J., Nakane, T., Forsberg, B.O., Kimanius, D., Hagen, W.J., Lindahl, E., and Scheres, S.H. (2018). New tools for automated high-resolution cryo-EM structure determination in RELION-3. eLife *7*. https://doi.org/10.7554/eLife.42166.

95. Scheres, S.H. (2012). RELION: implementation of a Bayesian approach to cryo-EM structure determination. J. Struct. Biol. *180*, 519–530.

96. Punjani, A., Zhang, H., and Fleet, D.J. (2020). Non-uniform refinement: adaptive regularization improves single-particle cryo-EM reconstruction. Nat. Methods *17*, 1214–1221.

97. Zivanov, J., Nakane, T., and Scheres, S.H.W. (2019). A Bayesian approach to beam-induced motion correction in cryo-EM single-particle analysis. IUCrJ *6*, 5–17.

98. Rosenthal, P.B., and Henderson, R. (2003). Optimal determination of particle orientation, absolute hand, and contrast loss in single-particle electron cryomicroscopy. J. Mol. Biol. *333*, 721–745.

99. Chen, S., McMullan, G., Faruqi, A.R., Murshudov, G.N., Short, J.M., Scheres, S.H., and Henderson, R. (2013). High-resolution noise substitution to measure overfitting and validate resolution in 3D structure determination by single particle electron cryomicroscopy. Ultramicroscopy *135*, 24–35.

100. Pettersen, E.F., Goddard, T.D., Huang, C.C., Couch, G.S., Greenblatt, D.M., Meng, E.C., and Ferrin, T.E. (2004). UCSF Chimera–a visualization system for exploratory research and analysis. J. Comput. Chem. *25*, 1605–1612.

101. Goddard, T.D., Huang, C.C., Meng, E.C., Pettersen, E.F., Couch, G.S., Morris, J.H., and Ferrin, T.E. (2018). UCSF ChimeraX: meeting modern challenges in visualization and analysis. Protein Sci. *27*, 14–25.

102. Emsley, P., Lohkamp, B., Scott, W.G., and Cowtan, K. (2010). Features and development of coot. Acta Crystallogr. D Biol. Crystallogr. *66*, 486–501.

103. Wang, R.Y., Song, Y., Barad, B.A., Cheng, Y., Fraser, J.S., and DiMaio, F. (2016). Automated structure refinement of macromolecular assemblies from cryo-EM maps using Rosetta. eLife *5*. https://doi.org/10.7554/eLife.17219.

104. Frenz, B., Rämisch, S., Borst, A.J., Walls, A.C., Adolf-Bryfogle, J., Schief, W.R., Veesler, D., and DiMaio, F. (2019). Automatically fixing errors in glycoprotein structures with Rosetta. Structure *27*, 134–139.e3.

105. Liebschner, D., Afonine, P.V., Baker, M.L., Bunkóczi, G., Chen, V.B., Croll, T.I., Hintze, B., Hung, L.W., Jain, S., McCoy, A.J., et al. (2019). Macromolecular structure determination using X-rays, neutrons and electrons: recent developments in Phenix. Acta Crystallogr. D Struct. Biol. *75*, 861–877.

106. Chen, V.B., Arendall, W.B., Headd, J.J., Keedy, D.A., Immormino, R.M., Kapral, G.J., Murray, L.W., Richardson, J.S., and Richardson, D.C. (2010). MolProbity: all-atom structure validation for macromolecular crystallography. Acta Crystallogr. D Biol. Crystallogr. *66*, 12–21.

107. Agirre, J., Iglesias-Fernández, J., Rovira, C., Davies, G.J., Wilson, K.S., and Cowtan, K.D. (2015). Privateer: software for the conformational validation of carbohydrate structures. Nat. Struct. Mol. Biol. *22*, 833–834.

108. Krissinel, E., and Henrick, K. (2007). Inference of macromolecular assemblies from crystalline state. J. Mol. Biol. *372*, 774–797.

109. Wentz, A.E., and Shusta, E.V. (2007). A novel high-throughput screen reveals yeast genes that increase secretion of heterologous proteins. Appl. Environ. Microbiol. *73*, 1189–1198.

110. Crawford, K.H.D., and Bloom, J.D. (2019). alignparse: a Python package for parsing complex features from high-throughput long-read sequencing. J. Open Source Softw. *4*, 4. https://doi.org/10.21105/joss.01915.

111. Millet, J.K., and Whittaker, G.R. (2016). Murine leukemia virus (MLV)-based coronavirus spike-pseudotyped particle production and infection. Bio Protoc. *6*, 6. https://doi.org/10.21769/BioProtoc.2035.

112. Greaney, A.J., Starr, T.N., Eguia, R.T., Loes, A.N., Khan, K., Karim, F., Cele, S., Bowen, J.E., Logue, J.K., Corti, D., et al. (2021). A SARS-CoV-2 variant elicits an antibody response with a shifted immunodominance hierarchy. Preprint at bioRxiv. https://doi.org/10.1101/2021.10.12.464114.

113. Sun, X., Yi, C., Zhu, Y., et al. (2022). Neutralization mechanism of a human antibody with pan-coronavirus reactivity including SARS-CoV-2. Nat Microbiol *7*, 1063–1074. https://doi.org/10.1038/s41564-022-01155-3.

STAR★METHODS

KEY RESOURCES TABLE

REAGENT or RESOURCE	SOURCE	IDENTIFIER
Antibodies		
Alexa Fluor® 647 AffiniPure Goat Anti-Mouse-IgG, Fcγ fragment specific	Jackson ImmunoResearch	Cat#115-605-008; RRID: AB_2338904
Alexa Fluor® 680 AffiniPure Goat Anti-Mouse IgG, light chain specific	Jackson ImmunoResearch	Cat#115-625-174; RRID: AB_2338937
Anti-C-Myc Antibody (Chicken) - FITC Conjugated	Immunology Consultants	Cat#CMYC-45F
Anti-VSV-M [23H12] Antibody	Kerafast	Cat#EB0011; RRID: AB_2734773
Goat anti-Human IgG Fc Secondary Antibody, HRP	Thermo Fisher Scientific - Invitrogen™	Cat#A18817; RRID: AB_2535594
Goat anti-Syrian Hamster IgG (H+L) Secondary Antibody, HRP	Thermo Fisher Scientific - Invitrogen™	Cat#PA1-28823; RRID: AB_10986856
Monoclonal ANTI-FLAG® M2 antibody produced in mouse	Sigma-Aldrich	Cat#F3165; RRID: AB_259529
R-Phycoerythrin AffiniPure Goat Anti-Human IgG, Fcγ fragment specific	Jackson ImmunoResearch	Cat#109-115-098; RRID: AB_2337675
Streptavidin, R-Phycoerythrin Conjugate (SAPE)	Thermo Fisher Scientific - Invitrogen	Cat#S866
S2M11	Tortorici et al.[58]	N/A
S309	Pinto et al.[56]	N/A
S2K146	Park et al.[45,50]	N/A
S2X324	Park et al.[45,50]	N/A
S2H97	Starr et al.[21]	N/A
76E1	Sun et al.[113]	N/A
RAY53	Silva et al.[51]	N/A
S2P6	Pinto et al.[52]	N/A
S2X259	Tortorici et al.[22]	N/A
S2X35	Piccoli et al.[49]	N/A
Bacterial and virus strains		
DH10B Competent Cells	Thermo Fisher Scientific	Cat#EC0113
Biological samples		
Cytiva HyClone™ Fetal Bovine Serum (Canada), Characterized	FisherScientific - Cytiva	Cat#SH3039603HI
SARS-CoV-2 HexaPro S/PRD-0038 HexaPro S vaccinated mouse sera	This study	N/A
VSV (G*ΔG-luciferase)	Kaname et al.[89]	N/A
Chemicals, peptides, and recombinant proteins		
AddaVax™	InvivoGen	Cat#vac-adx-10
Biotinylated Human ACE2 / ACEH Protein, His, Avitag™	AcroBiosystems	Cat#AC2-H82E6
CHAPSO	Anatrace	N/A
iBright™ Prestained Protein Ladder	Thermo Fisher Scientific - Invitrogen™	Cat#LC5615
Octet ® Kinetics Buffer 10X	Sartorius	Cat#18-1105
Poly-L-lysine solution	Sigma-Aldrich	Cat#P4707
SureBlue™ TMB 1-Component Microwell Peroxidase Substrate	Seracare Life Sciences Inc	Cat#50-674-93

(*Continued on next page*)

Continued

REAGENT or RESOURCE	SOURCE	IDENTIFIER
Critical commercial assays		
Bulk BirA - Bulk BirA: BirA biotin-protein ligase bulk reaction kit	Avidity	N/A
Charles River limulus amebocyte lysate (LAL) cartridges	Charles River	Cat#PTS201F
ExpiFectamine™ 293 Transfection Kit	Thermo Fisher Scientific - Gibco™	Cat#A14525
Lipofectamine™ 2000 Transfection Reagent	Thermo Fisher Scientific - Invitrogen™	Cat#11668500
ONE-Glo™ EX Luciferase Assay System	Promega	Cat#E8150
Deposited data		
PRD-0038 RBD – *R. alcyone* ACE2 cryoEM map	https://www.ebi.ac.uk/emdb/	EMD: 41786
PRD-0038 RBD – *R. alcyone* ACE2 local refinement cryoEM map	https://www.ebi.ac.uk/emdb/	EMD: 41784
PRD-0038 RBD – *R. alcyone* ACE2 local refinement atomic model	https://www.rcsb.org/	PDB: 8U0T
PRD-0038 S cryoEM map	https://www.ebi.ac.uk/emdb/	EMD: 41842
PRD-0038 S atomic model	https://www.rcsb.org/	PDB: 8U29
PRD-0038 S NTD local refinement cryoEM map	https://www.ebi.ac.uk/emdb/	EMD: 41843
Raw CCS reads	NCBI Sequence Read Archive	BioProject PRJNA962117, BioSample SAMN34384156
Sequencing reads on RBD expression	NCBI Sequence Read Archive	BioProject PRJNA962117, BioSample SAMN34384823
Raw Illumina sequencing data on sera DMS	NCBI Sequence Read Archive	BioProject PRJNA714677, BioSample SAMN36715819
Interactive DMS heatmaps of change in binding avidity to ACE2-Fc orthologs	https://tstarrlab.github.io/SARSr-CoV-RBD_DMS/RBD-heatmaps_delta/	N/A
Binding curves from sera binding to a pan-sarbecovirus library of yeast-displayed RBDs using high-throughput FACS-seq assay	https://github.com/tstarrlab/SARSr-CoV_MAP_PRD0038-vaccine/blob/main/results/summary/compute_AUC.md#plot-all-curves	N/A
Complete pipeline for DMS of mutational effects on ACE2 binding	https://github.com/tstarrlab/SARSr-CoV-RBD_DMS/blob/main/results/summary/summary.md	N/A
Table of each N16 barcode linked to its unique RBD mutant (PRD-0038)	https://github.com/tstarrlab/SARSr-CoV-RBD_DMS/blob/main/results/variants/codon_variant_table_PRD0038.csv	N/A
Table of each N16 barcode linked to its unique RBD mutant (SARS1)	https://github.com/tstarrlab/SARSr-CoV-RBD_DMS/blob/main/results/variants/codon_variant_table_SARS1.csv	N/A
Table of counts of each barcode in each FACS bin	https://github.com/tstarrlab/SARSr-CoV-RBD_DMS/blob/main/results/counts/variant_counts.csv.gz	N/A
Computational pipelines for computing per-barcode binding constants	https://github.com/tstarrlab/SARSr-CoV-RBD_DMS/blob/main/results/summary/compute_binding_Kd_huACE2.md	N/A
Computational pipelines for computing per-barcode expression phenotypes	https://github.com/tstarrlab/SARSr-CoV-RBD_DMS/blob/main/results/summary/compute_expression_meanF.md	N/A

(*Continued on next page*)

Continued

REAGENT or RESOURCE	SOURCE	IDENTIFIER
Final mutant phenotype as the average of per-barcode	https://github.com/tstarrlab/SARSr-CoV-RBD_DMS/blob/main/results/summary/collapse_barcodes_lib40_41.md	N/A
Final per-mutant deep mutational scanning phenotype	https://github.com/tstarrlab/SARSr-CoV-RBD_DMS/blob/main/results/final_variant_scores/final_variant_scores_lib40_41.csv	N/A
Complete pipeline of DMS of vaccinated sera	https://github.com/tstarrlab/SARSr-CoV_MAP_PRD0038-vaccine/blob/main/results/summary/summary.md	N/A
Barcode reads mapped to library barcodes with raw counts (sera DMS)	https://github.com/tstarrlab/SARSr-CoV_MAP_PRD0038-vaccine/blob/main/results/counts/variant_counts.csv	N/A
AUC calculation for each library barcode (sera DMS)	https://github.com/tstarrlab/SARSr-CoV_MAP_PRD0038-vaccine/blob/main/results/summary/compute_AUC.md	N/A
Per-barcode AUC metrics (sera DMS)	https://github.com/tstarrlab/SARSr-CoV_MAP_PRD0038-vaccine/blob/main/results/bc_sera_binding/bc_sera_binding.csv	N/A
Final variant derivation (sera DMS)	https://github.com/tstarrlab/SARSr-CoV_MAP_PRD0038-vaccine/blob/main/results/summary/collapse_barcodes_SARSr-DMS.md	N/A
Final per-variant serum-binding values (WTS)	https://github.com/tstarrlab/SARSr-CoV_MAP_PRD0038-vaccine/blob/main/results/final_variant_scores/final_variant_scores_wts.csv	N/A
Final per-variant serum-binding values (DMS)	https://github.com/tstarrlab/SARSr-CoV_MAP_PRD0038-vaccine/blob/main/results/final_variant_scores/final_variant_scores_dms.csv	N/A
Experimental models: Cell lines		
Expi293F™ cells	Thermo Fisher Scientific - Gibco™	Cat#A14527
HEK293T with stable human ACE2 expression	Crawford et al.[88]	N/A
HEK293T/17 cells	ATCC	Cat#CRL-11268
I1-mouse Hybridoma	ATCC	Cat#CRL-2700
Experimental models: Organisms/strains		
Mouse: Female BALB/c	Envigo	N/A
Yeast: AWY101 *S. cerevisiae*	Wentz and Shusta[109]	N/A
Oligonucleotides		
Recombinant DNA		
pCMVR::PRD-0038 RBD WT HisAvi	This study	N/A
pCMVR::PRD-0038 RBD K482Y HisAvi	This study	N/A
pCMVR::PRD-0038 RBD T487W HisAvi	This study	N/A
pCMVR::PRD-0038 RBD K482Y/T487W HisAvi	This study	N/A
pTwsitCMV::human ACE2 Fc	Starr et al.[76]	N/A
pCMV::*R. alcyone* ACE2 Fc HisAvi	This study	N/A
pCMV::*R. landeri* ACE2 Fc HisAvi	This study	N/A

(*Continued on next page*)

Continued

REAGENT or RESOURCE	SOURCE	IDENTIFIER
pCMV::*R. affinis* ACE2 Fc 9479 HisAvi	Starr et al.[29,38,79]	N/A
pCMV::*R. affinis* ACE2 Fc 787 HisAvi	Starr et al.[29,38,79]	N/A
pCMV::*R. sinicus* ACE2 Fc 3364 HisAvi	Starr et al.[29,38,79]	N/A
pCMV::*R. sinicus* ACE2 Fc WJ4 HisAvi	Starr et al.[29,38,79]	N/A
pCMV::*R. sinicus* ACE2 Fc HisAvi	Starr et al.[29,38,79]	N/A
pCMV::*R. sinicus* ACE2 Fc 1446 HisAvi	Starr et al.[29,38,79]	N/A
pCMV::*R. sinicus* ACE2 Fc WJ1 HisAvi	Starr et al.[29,38,79]	N/A
pCMV::*R. sinicus* ACE2 Fc 1434 HisAvi	Starr et al.[29,38,79]	N/A
pCMV::*R. sinicus* ACE2 Fc 3358 HisAvi	Starr et al.[29,38,79]	N/A
pCMV::*R. sinicus* ACE2 Fc 1438 HisAvi	Starr et al.[29,38,79]	N/A
pCMVR::*R. alcyone* ACE2 ecto dimer	This study	N/A
pCMV::*R. alcyone* ACE2 His	This study	N/A
pCMV::*R. landeri* ACE2 His	This study	N/A
pCMVR::PRD-0038 S ecto PentaPro HisAvi	This study	N/A
pCMVR::PRD-0038 S ecto HexaPro HisAvi	This study	N/A
pHDM::PRD-0038 S full length WT del21 3xFLAG	This study	N/A
pHDM::PRD-0038 S full length K482Y del21 3xFLAG	This study	N/A
pHDM::PRD-0038 S full length T487W del21 3xFLAG	This study	N/A
pHDM::PRD-0038 S full length K482Y/T487W del21 3xFLAG	This study	N/A
pcDNA3.1(-)::SARS-CoV-2 S ecto HexaPro AviHis	Hsieh et al. (2020)[55]	N/A
pHDM::*R. affinis* ACE2 9479 full length	This study	N/A
pHDM::*R. affinis* ACE2 787 full length	This study	N/A
pHDM::*R. sinicus* ACE2 3364 full length	This study	N/A
pHDM::*R. sinicus* ACE2 WJ4 full length	This study	N/A
pHDM ::*R. sinicus* ACE2 full length	This study	N/A
pHDM::*R. sinicus* ACE2 1446 full length	This study	N/A
pHDM::*R. sinicus* ACE2 WJ1 full length	This study	N/A
pHDM::*R. sinicus* ACE2 1434 full length	This study	N/A
pHDM::*R. sinicus* ACE2 3358 full length	This study	N/A
pHDM::*R. sinicus* ACE2 1438 full length	This study	N/A
pHDM::*R. alcyone* ACE2 full length	This study	N/A
pHDM::*R. landeri* ACE2 full length	This study	N/A
pHDM::*R. ferrumequinum* XM_033107295.1 ACE2 full length	This study	N/A
pHDM::*R. ferrumequinum* FJ598617.1 ACE2 full length	This study	N/A
pHDM::SARS-CoV-2 D614G S full length del21	Crawford et al.[88]	N/A
pHDM::SARS-CoV-2 BA.2 S full length del21	Bowen et al.[60,75]	N/A
pHDM::SARS-CoV-2 BA.5 S full length del21	Bowen et al.[60,75]	N/A
pcDNA3.1(-)::RaTG13 S full length	Walls et al.[84]	N/A
pcDNA3.1(-)::SARS-CoV-1 S full length	Millet and Whittaker[111]	N/A
pHDM::Khosta-1 S full length del21	This study	N/A
Software and algorithms		
Alignparse (v.0.2.4)	Crawford and Bloom[110]	N/A

(*Continued on next page*)

Continued

REAGENT or RESOURCE	SOURCE	IDENTIFIER
Coot	Emsley et al.[102]	https://www2.mrc-lmb.cam.ac.uk/personal/pemsley/coot/
CryoSPARC	Punjani et al.[93]	https://cryosparc.com
GraphPad Prism	GraphPad Software	www.graphpad.com
Leginon	Suloway et al.[91]	https://emg.nysbc.org/redmine/projects/leginon/wiki/Leginon_Homepage
Molprobity	Chen et al.[106]	http://molprobity.manchester.ac.uk/
Octet Data Analysis HT software	Sartorius	https://www.sartorius.com/en/products/protein-analysis/octet-bli-detection/octet-systems-software
Phenix	Liebschner et al.[105]	http://www.phenix-online.org/
Pisa	Krissinel and Henrick[108]	http://www.ebi.ac.uk/msd-srv/prot_int/pistart.html
Privateer	Agirre et al.[107]	http://www.ccp4.ac.uk/html/privateer.html
Relion	Zivanov et al.[94]	https://www3.mrc-lmb.cam.ac.uk/relion
Rosetta	Wang et al.,[103] Frenz et al.[104]	https://www.rosettacommons.org/software
UCSF Chimera	Pettersen et al.[100]	https://www.rbvi.ucsf.edu/chimera
UCSF ChimeraX	Goddard et al.[101]	https://www.rbvi.ucsf.edu/chimerax/
WARP	Tegunov and Cramer[92]	http://www.warpem.com/warp/
Other		
Amicon® Ultra-15 Centrifugal Filter Unit (100kDa)	Millipore	Cat#UFC9100
C-flat™ 2/2 on 200 copper mesh	Electron Microscopy Sciences	N/A
Corning™ BioCoat™ Poly-D-Lysine Culture Dish	FisherScientific - Corning	Cat#08-774-262
Corning® Spin-X® UF concentrators (100kDa)	MilliporeSima - Corning	Cat#CLS431491
HisTrap HP His tag protein purification columns	Cytiva	Cat#17524701
HiTrap Protein A HP antibody purification columns	Cytiva	Cat#17040201
MilliporeSigma™ Amicon™ Ultra-15 Centrifugal Filter Units (10kDa)	MilliporeSigma™	Cat#UFC901008
Penicillin-Streptomycin (10,000 U/mL)	Thermo Fisher Scientific - Gibco™	Cat#15140163
Superose™ 6 Increase 10/300 GL	Cytiva	Cat#29091596
UltrAuFoil® R 2/2, 200 mesh, Au grid	Electron Microscopy Sciences	N/A

RESOURCE AVAILABILITY

Lead contact

Further information and requests for resources and reagents should be directed to and will be fulfilled by the lead contact, David Veesler (dveesler@uw.edu)

Materials availability

Materials generated in this study will be made available on request after signing a materials transfer agreement with the University of Washington.

Data and code availability

Data reported in this paper will be shared by the lead contact upon request. CryoEM maps and model data have been deposited at EMDB and PDB, respectively, and are publicly available as of the date of publication with accession numbers listed in the Key resources table. Raw sequencing data are available on the NCBI Sequence Read Archive and accession numbers are listed in the key resources table. DMS data and all original code has been deposited at GitHub and are publicly available as of the date of publication. DOIs are listed in the key resources table, figure legends, and method section. Any additional information required to reanalyze the data reported in this paper is available from the lead contact upon request.

EXPERIMENTAL MODEL AND STUDY PARTICIPANT DETAILS

Cell lines

Cell lines used in this study were obtained from DH10B competent cells (Thermo Fisher Scientific), HEK293T (ATCC, CRL-11268) and Expi293F (Thermo Fisher Scientific, A14527) except for the HEK293T cells with stable human ACE2 expression which was kindly provided by Jesse Bloom.[88] Cells were cultured in 10% FBS (Fisher Scientific-Cytiva), 1% penicillin-streptomycin (Thermo Fisher Scientific) DMEM at 37°C, 5% CO_2. AWY101 *S. cerevisiae* strain was used for yeast surface-display experiments. None of the cell lines were authenticated or tested for mycoplasma contamination.

In vivo animal studies

Female BALB/c mice were purchased from Envigo (order code 047) at 7 weeks of age and were maintained in a specific pathogen-free facility within the Department of Comparative Medicine at the University of Washington, Seattle, accredited by the Association for Assessment and Accreditation of Laboratory Animal Care (AAALAC). Animal experiments were conducted in accordance with the University of Washington's Institutional Animal Care and Use Committee.

METHOD DETAILS

Production of recombinant PRD-0038 RBDs

The PRD-0038 S glycoprotein sequence was obtained from Genbank (MT726045). Both wildtype and mutant PRD-0038 RBDs (residues 318-520) were synthesized by GenScript with an N-terminal mu-phosphatase signal peptide and C-terminal 8x His tag, a short linker (GGSS) followed by an Avi tag in a pCMVR plasmid and sub-cloned with E. coli DH10B Competent Cells. Expi293F cells were grown at 37°C with 8% CO_2 and DNA transfections were conducted with the ExpiFectamine 293 Transfection Kit (Thermo Fisher Scientific). Cell culture supernatants were harvested three days post transfection. RBDs were purified using nickel based affinity chromatography using HisTrap™ High Performance column (Cytiva). Proteins were first washed with 10 column volumes of a buffer containing 25mM sodium phosphate (pH8.0) and 300 mM NaCl, before elution with 8 column volumes of a buffer containing 25 mM sodium phosphate (pH8.0), 300 mM NaCl, 500mM imidazole. Eluted proteins were buffer exchanged into 1x PBS (137mM NaCl, 2.7mM KCl, 10mM Na2HPO4, 1.8mM KH2PO4, pH 8.0) using Amicon Ultra-15 Centrifugal Filter Unit (10 kDa) (Millipore). Overnight biotinylation reactions were performed using the BirA Biotin-Protein Ligase Kit (Avidity) at 4°C in 1x BiomixA, BiomixB. Biotinylated proteins were once again affinity purified using the HisTrap column as previously described to get rid of BirA. Once purified, buffer exchanged into PBS, and concentrated, proteins were flash-frozen and stored at -80°C until use.

Production of recombinant ACE2 ectodomains

Genbank accession numbers for all ACE2s can be found in Table S1. Recombinant ACE2 ectodomain constructs were synthesized by GenScript. ACE2-His ectodomain constructs comprise of residues 19–615 with an N-terminal mu-phosphatase signal peptide and C-terminal 8x His tag, a short GGSS linker, and an Avi tag. ACE2-Fc ectodomain[76] constructs comprise residues 19–615 with an N-terminal mu-phosphatase signal peptide and C-terminal fusion to a sequence encoding a thrombin cleavage site, a short linker (GGGG) and a human Fc fragment and were cloned in a pCMV plasmid. The native *R. alcyone* ACE2 ectodomain dimer comprises residues 1-740 and a C-terminal 8x His tag, a GGSS linker and an Avi tag and was cloned in a pCMVR plasmid. All ACE2 orthologue ectodomains were produced in Expi293F cells at 37°C supplemented and 8% CO_2. Transfections were performed with the ExpiFectamine 293 Transfection Kit (Thermo Fisher Scientific). Cell culture supernatants were harvested four days after transfection and proteins were purified using HiTrap Protein A HP (Cytiva) or HisTrap™ High Performance column (Cytiva). ACE2-Fc proteins were first washed with 10 column volumes of 20 mM sodium phosphate (pH8.0) then eluted with 0.1 M citric acid (pH 3.0) directly into tubes containing 1M Tris-HCl (pH 9.0). Purified proteins were buffer exchanged into PBS (pH 8.0), concentrated using Spin-X® UF 20 mL Centrifugal Concentrator, 100,000 MWCO Membrane (PES) (Corning), and flash-frozen. ACE2-His proteins were washed with 10 column volumes of a buffer containing 25 mM sodium phosphate (pH 8.0), 300 mM NaCl, then eluted with 8 column volumes of a buffer containing 25 mM sodium phosphate (pH 8.0), 300 mM NaCl and 500 mM imidazole. Eluted proteins were buffer exchanged into 1x PBS (pH8.0) using Amicon Ultra-15 Centrifugal Filter Unit (10 kDa) (Millipore) and flash-frozen.

Production of recombinant PRD-0038 PentaPro S, HexaPro S, and SARS-CoV-2 HexaPro S

The PRD-0038 S glycoprotein sequence was obtained from Genbank (MT726045). Recombinant PRD-0038 S glycoprotein ectodomain (residues 16-1194) constructs with pre-fusion stabilizing mutations (PentaPro: F800P, S882P, S925P, K969P, V970P or

HexaPro: F800P, A875P, S882P, S925P, K969P, V970P) were synthesized by GenScript with an N-terminal mu-phosphatase signal peptide and C-terminal short linker (SG), TEV protease site (RENLYFQ), a short linker (GGGGSG), Foldon, 8x His tag, a short linker (GGSS) followed by an Avi tag in a pCMVR plasmid. The SARS-CoV-2 S glycoprotein ectodomain construct comprises residues 1-1208 with the native signal peptide, the HexaPro prefusion stabilizing mutations[55] (F817P, A892P, A899P, A942P, K986P, V987P), abrogation of the furin cleavage site (residues 682-685, GSAS) and a C-terminal short linker (GSG), followed by a foldon, HRV 3C site (LEVLFQGP), a short linker (GSG), an avi tag, a short linker (GSG), an 8x his tag in a pcDNA3.1(-) plasmid. Expi293F cells were grown at 37°C with 8% CO_2 and DNA transfections were conducted with the ExpiFectamine 293 Transfection Kit (Thermo Fisher Scientific). Cell culture supernatants were harvested four days post-transfection and proteins were purified using HisTrap™ High Performance column (Cytiva). Proteins were first washed with 10-15 column volumes of a buffer containing 25 mM sodium phosphate, 300 mM NaCl, 20 mM imidazole, pH 8.0, followed by elution with 10-15 column volumes using 300 mM imidazole, pH 8.0. Eluted proteins were concentrated and buffer exchanged into 1x PBS or 1x TBS (20 mM Tris, 150 mM NaCl, pH 8.0) using Amicon Ultra-15 Centrifugal Filter Unit (100 kDa) (Millipore). Purified proteins were snap frozen and stored at -80°C. Purified proteins were checked for endotoxin level using Charles River Limulus Amebocyte Lysate (LAL) cartridges (Charles River, PTS201F). Endotoxin-free SARS-CoV-2 HexaPro S and PRD-0038 HexaPro S were flash-frozen and stored at -80°C until the day of immunization.

Production of PRD-0038 wild-type RBD- Natively Dimerized R. alcyone Complex

For complex formation, wild-type PRD-0038 RBD was mixed with natively dimerized R. alcyone ACE2 His at a 4:1 molar ratio, then incubated at room temperature for 5-10 min. Gel filtration was performed to remove excess RBD on a Superose 6 10/300 GL column (Cytiva) equilibrated in 50 mM Tris-HCl, 150 mM NaCl. Complex formation was confirmed by SDS-PAGE, and the PRD-0038 RBD- R. alcyone ACE2 complex was snap frozen and stored at -80°C until day of grid preparation.

Binding analysis using biolayer interferometry (BLI)

BLI binding assays were performed on an Octet Red (Sartorius) instrument operated at 30°C with shaking (1000 rpm). For biotinylated RBD and ACE2-Fc or ACE2-His binding assays, streptavidin biosensors were hydrated in water for 10 min prior to the experiment. Biosensors were incubated in 10x kinetics buffer (Sartorius) for 60s followed by the loading of biotinylated RBDs to the tip, all to a final level of 1 nm. Loaded biosensors were equilibrated in 10x kinetics buffer for 120s which served as our baseline. For avidity binding assays, association with 1 μM ACE2-Fc (dimeric form) was performed for 300 s followed by 300 s of dissociation in 10x kinetics buffer. For affinity binding assays to determine K_D values, RBD-loaded tips were dipped into a concentration series of ACE2-His (2 fold serial dilution from 100 nM to 6.25 nM for *R. alcyone* ACE2-His, 3 fold serial dilution from 660 nM to 8 nM for *R. landeri* ACE2-His) for 600 s followed by 600 s of dissociation in 10x kinetics buffer. Global fits were used to calculate K_D values using a 1:1 binding fit model. Data were plotted using GraphPad Prism. Assays were replicated with three biological replicates (recombinant RBD proteins generated on different days) and representative graphs are shown.

Production of VSV pseudoviruses

Wildtype and mutant PRD-0038 S constructs consisting of residues 1-1235 and containing a 21 residue C-terminal deletion (del21) followed by a 3x FLAG tag were synthesized by GenScript and placed into an HDM plasmid. VSV pseudoviruses were produced using HEK293T cells seeded on BioCoat Cell Culture Dish : poly-D-Lysine 100 mm (Corning). Cells were transfected with PRD-0038 S-Flag constructs using Lipofectamine 2000 (Thermo Fisher Scientific) in Opti-MEM transfection medium. After 5h of incubation at 37 °C with 5% CO2, cells were supplemented with DMEM containing 10% of FBS. On the next day, cells were infected with VSV (G*ΔG-luciferase)[89] for 2h, followed by five time wash with DMEM medium before addition of anti-VSV G antibody (I1-mouse hybridoma supernatant diluted 1:40, ATCC CRL-2700) and medium. After 18-24 h of incubation at 37 °C with 5% CO_2, pseudoviruses were collected and cell debris removed by centrifugation at 3,000xg for 10 min. Pseudoviruses were further filtered using a 0.45 μm syringe filter and concentrated 25-50x prior to storage at -80°C. Mock VSV pseudoviruses were prepared as above but without S transfection.

Cell entry assays comparing wildtype and mutant PRD-0038 S VSV pseudoviruses

HEK293T cells were transfected with full length *Rhinolophus* ACE2 orthologs using Lipofectamine 2000 (Thermo Fisher Scientific) in Opti-MEM five hours prior to plating into 96-well plates [3610] (Corning) coated with poly-lysine [P4707] (Sigma) and incubated 18-24 h before infection with VSV pseudoviruses. For human ACE2 entry assays, HEK293T cells with stable hACE2 expression were plated into poly-lysine-coated 96-well plates and incubated for 18-24h before infection with VSV pseudoviruses. The amount of pseudovirus used for infection was adjusted using Western Blot based on S incorporation across different mutants to use a constant input of S. Detection of VSV backbone was performed with 1:1,000 Anti-VSV-M [23H12] Antibody (Kerafast). Detection of 3x-FLAG tagged S was performed with 1:400 monoclonal ANTI-FLAG® M2 antibody [F3165] produced in mouse (Sigma). 1:50,000 Alexa Fluor® 680 AffiniPure Goat Anti-Mouse IgG [115-625-174] (Jackson ImmunoResearch) was used as the secondary antibody. A representative Western Blot is shown in Figure S4E. Genbank accession numbers for all ACE2s can be found in Table S1. After 1h of infection, an additional 40 μL of DMEM supplemented with 20% FBS and 2% PenStrep was added to the cells. After 18–20h, 40 μL of One-Glo-EX substrate (Promega) was added to each well and incubated on a plate shaker in the dark for 5 min before

reading the relative luciferase units using a BioTek Neo2 plate reader. Fold change of relative luciferase units over mock VSV were plotted in Prism (GraphPad) with mock being cells that were not transfected with an S-encoding plasmid. 3 biological replicates, each of which with 3 technical replicates were carried out.

Cell entry assay for PRD-0038 S VSV with distinct *Rhinolophus* ACE2s

For wildtype PRD-0038 S VSV entry into HEK293T cells transfected with *R. affinis*, *R. sinicus*, *R. landeri*, and *R. alcyone* alleles full-length ACE2 alleles (Figure 1D), HEK293T cells (ATCC) were cultured in 10% FBS, 1% penicillin–streptomycin DMEM at 37 °C in a humidified 5% CO_2 incubator. Cells were plated 18-24 hours prior to transfection into 96-well plates [3610] (Corning) coated with poly-lysine [P4707] (Sigma). All transfections were performed using full-length *Rhinolophus* ACE2 placed into a HDM plasmid (synthesized by GenScript). Transfection of ACE2 alleles into HEK293T cells was performed using 0.2 μg DNA and 0.15 μL Lipofectamine 2000 (Thermo Fisher Scientific) per well in Opti-MEM. After a 5 h incubation at 37 °C in a humidified 8% CO_2 incubator, DMEM was added to obtain a final concentration of 10% FBS and 1% penicillin–streptomycin. Cells were incubated at 37 °C in a humidified 8% CO_2 incubator for 36–48 h prior to infection. For each infection test, 2-3 technical replicates were performed, and the assays were repeated on a second day, for a total of 4-6 technical replicates. Three biological replicates (pseudovirus generated on different days) were used for cell entry and each point shown represents the mean fold change for each biological replicate. Results were plotted using Graphpad Prism (Figure 1D). Genbank accession numbers for all ACE2s can be found in Table S1.

Cryo-EM sample preparation and data collection

Cryo-EM grids of PRD-0038 PentaPro S were prepared using two separate methods and data were combined during data processing. The first dataset was collected from the grids prepared using a reverse grid-blotting method. 3 μL of sample was added to the carbon side of a glow discharged C-flat R2/2 copper grid and 1μL was added to the back side before addition of 1 μL of CHEMS lipid dissolved in chloroform on the front side. The sample was allowed to sit on the grid for 1 minute and then manually blotted from the back side using a strip of Whatman #1 filter paper and plunged into liquid ethane. The second dataset was collected from a lacey carbon grid with a thin home-made continuous carbon layer. 3 μL of 0.15 mg/mL PRD-0038 Pentapro S was loaded onto the glow discharged (6s at 20mA) grid followed by plunge freezing using a vitrobot MarkIV (ThermoFisher Scientific). The grid was blotted with a blot force of -1, 3 second blot time, and 10 second wait time before the plunge freeze at 100% humidity and 25 °C. For the PRD-0038 RBD-ACE2 complex, grids were prepared by applying 3 μL of 4 mg/ml PRD-0038 RBD bound to the *R. alcyone* ACE2 dimer with 7 mM CHAPSO (Anatrace) were applied and blotted twice as previously described,[90] onto freshly glow discharged R 2/2 UltrAuFoil grids prior to plunge freezing using a vitrobot MarkIV (ThermoFisher Scientific) with a blot force of 0 and 5 sec blot time at 100 % humidity and 22°C. Data were acquired using an FEI Titan Krios transmission electron microscope operated at 300 kV and equipped with a Gatan K3 direct detector and Gatan Quantum GIF energy filter, operated in zero-loss mode with a slit width of 20 eV. Automated data collection was carried out using Leginon[91] at a nominal magnification of 105,000x with a pixel size of 0.843 Å. The dose rate was adjusted to 15 counts/pixel/s, and each movie was acquired in counting mode fractionated in 75 frames of 40 ms. A total of 2,482 and 11,743 micrographs were collected for the PRD-0038 S and PRD-0038 RBD-ACE2 datasets, respectively.

Cryo-EM data processing, model building and refinement

Motion correction, contrast-transfer function (CTF) parameter estimation, automatic particle picking, and extraction were performed using Warp[92] for each data set. For the PRD-0038 S structure, particle images were extracted with a box size of 260 pixels with a pixel size of 1.686Å. After two rounds of 2D classification using cryoSPARC,[93] well-defined particles were selected and particles from each dataset were combined and binned to a box size of 130 pixels with a pixel size of 3.372Å for subsequent 3D classification using Relion[94,95] with 50 iterations (angular sampling 7.5° for 25 iterations and 1.8° with local search for 25 iterations). 103,347 particles were selected and re-extracted with a box size of 260 and pixel size of 1.686Å for cryoSPARC non-uniform refinement[96] with C3 symmetry and further subjected to Bayesian polishing[97] in Relion. Finally, another round of non-uniform refinement with C3 symmetry and optimized per-particle defocus was carried out to the polished particles. To improve the density of the NTD, we used symmetry expansion and local refinement using cryoSPARC. For the PRD-0038 RBD - *R. alcyone* ACE2 structure, two rounds of reference-free 2D classification were performed using cryoSPARC to select well-defined particle images. These selected particles were subjected to two rounds of 3D classification with 50 iterations each (angular sampling 7.5° for 25 iterations and 1.8° with local search for 25 iterations) using Relion with an initial model generated with ab-initio reconstruction in cryoSPARC. 3D refinements were carried out using non-uniform refinement along with per-particle defocus refinement in CryoSPARC. To improve the density of the RBD-ACE2 dimer, the particles were subjected to cryoSPARC heterogeneous refinement. Particles belonging to classes with the best resolved RBD-ACE2 density were selected and subjected to the Bayesian polishing procedure implemented in Relion before performing another round of non-uniform refinement in cryoSPARC followed by per-particle defocus refinement and again non-uniform refinement. To further improve the density of the RBD-ACE2 domains, the particles were symmetry expanded and subjected to focus 3D classification without refining angles and shifts using a soft mask encompassing the RBD and monomer ACE2 using a tau value of 40 in Relion. Particles belonging to classes with the best resolved RBD-ACE2 density were selected and then subjected to local refinement using CryoSPARC. Local resolution estimation, filtering, and sharpening were carried out using CryoSPARC. Reported resolutions are based on the gold-standard Fourier shell correlation (FSC) of 0.143 criterion and Fourier shell correlation curves were corrected for the effects of soft masking by high-resolution noise substitution.[98,99] UCSF Chimera,[100] UCSF ChimeraX,[101] and Coot[102] were used to fit atomic models into the cryoEM maps. S and RBD-ACE2 models were refined and relaxed using Rosetta[103,104] using

sharpened and unsharpened maps and validated using Phenix,[105] Molprobity[106] and Privateer.[107] Analysis of interface residues was assisted by PISA.[108]

Monoclonal antibody ELISAs

For PRD-0038 HexaPro S and SARS-CoV-2 HexaPro S ELISAs, 30 μl of the proteins at 3 μg/mL were plated onto 384-well Nunc Maxisorp plate (ThermoFisher, 464718) in 1x TBS and incubated 1h at 37°C followed by slap drying and blocking with 80 μL of Casein for 1 h at 37°C. After incubation, plates were slap dried and 1:4 serial dilutions of the corresponding mAbs starting from 0.1 mg/ml were made in 30 μl TBST, added to the plate and incubated at 37°C for 1 h. Plates were washed 4x in TBST and 30 μl of 1:5,000 Goat anti-Human IgG Fc Secondary Antibody, HRP (Thermo Fisher, A18817) or Goat anti-Syrian Hamster IgG (H+L) Secondary Antibody, HRP (Thermo Fisher, PA1-28823) were added to each well and incubated at 37°C. After 1 h, plates were washed 4x in TBST and 30 μl of TMB (SeraCare) was added to every well for 2 min at room temperature. Reactions were quenched with the addition of 30 μl of 1N HCl. Plates were immediately read at 450 nm on a BioTek Neo2 plate reader and data plotted and fit in Prism 9 (GraphPad) using nonlinear regression sigmoidal, 4PL, X is the concentration to determine EC_{50} values from curve fits.

Deep mutational scanning for mutational effects on ACE2 binding

The complete deep mutational scanning pipeline can be found at: https://github.com/tstarrlab/SARSr-CoV-RBD_DMS/blob/main/results/summary/summary.md. Deep mutational scanning libraries for sarbecovirus strains including PRD-0038 and SARS-Cov-1 Urbani were constructed as previously described.[79] Briefly, site-saturation mutagenesis libraries spanning all RBD positions were produced by Twist Bioscience (or NNS mutagenesis for positions that failed Twist mutagenesis), tagged with an N16 barcode, and cloned into a yeast display vector backbone via Gibson Assembly. Libraries were electroporated into *E. coli* and plated at a target bottleneck of 40,000 unique barcodes per library to overrepresent the ~4,000 possible amino acid mutations. Colonies were scraped from each transformation plate, library plasmid purified, and transformed into the AWY101 *S. cerevisiae* strain[109] for yeast surface-display experiments. Library plasmids were sequenced using a PacBio Sequel IIe to generate long sequence reads spanning the N16 barcodes and RBD coding sequence. Raw CCS reads are available on the NCBI Sequence Read Archive, BioProject PRJNA962117, BioSample SAMN34384156. Reads were processed using alignparse (version 0.2.4)[110] to generate a table linking each N16 barcode to its unique RBD mutant, available at: https://github.com/tstarrlab/SARSr-CoV-RBD_DMS/blob/main/results/variants/codon_variant_table_PRD0038.csv and https://github.com/tstarrlab/SARSr-CoV-RBD_DMS/blob/main/results/variants/codon_variant_table_SARS1.csv.

The RBD expression level and ACE2-binding avidity of each RBD mutant was determined via high-throughput FACS-seq assays as previously described.[79] ACE2-binding titrations were performed by incubating induced yeast-display libraries with a concentration series of dimeric ACE2 ligands from 10^{-6} to 10^{-13} M at 1-log intervals, plus a 0 M ACE2 sample, with samples equilibrated overnight at room temperature with mixing. Yeast were washed with PBS-BSA (0.2 mg/L), labeled with 1:100 FITC-conjugated chicken anti-Myc (Immunology Consultants CMYC-45F) to detect yeast-displayed RBD and 1:200 PE-conjugated streptavidin (Thermo Fisher S866) or goat anti-human-IgG (Jackson ImmunoResearch 109-115-098) to detect binding of biotinylated (human, Acro Biosystems H82E6) or Fc-tagged (*R. alcyone*, *R. landeri*) ACE2. For each titration sample, RBD^+ yeast were fractionated into four bins of PE fluorescence (ACE2 binding), grown overnight, plasmid isolated, N16 barcode amplified, and barcodes counted via high-throughput sequencing on an Illumina NextSeq. RBD expression was measured by sorting cells into four bins on the basis of Myc-FITC labeling, followed by outgrowth, plasmid isolation, N16 barcode amplification, and sequencing. Sequencing reads are available on the NCBI Sequence Read Archive, BioProject PRJNA962117, BioSample SAMN34384823.

Demultiplexed Illumina barcode reads were aligned to library barcodes using dms_variants (version 0.8.9), yielding a table of counts of each barcode in each FACS bin which is available at https://github.com/tstarrlab/SARSr-CoV-RBD_DMS/blob/main/results/counts/variant_counts.csv.gz. Reads were downweighted by the ratio of total sequence reads from a bin to the number of cells sorted into that bin. For each barcode, we inferred the apparent dissociation constant for avid binding ($K_{D,app}$) by fitting the standard non-cooperative Hill equation to the mean FACS bin of a barcode variant as a function of ACE2 concentration. For each barcode, expression was determined via a maximum likelihood estimator of log-MFI based on the distribution of barcode counts across FACS bins and the known fluorescence boundaries of those bins. The computational pipelines for computing per-barcode binding constants and expression phenotypes are available at: https://github.com/tstarrlab/SARSr-CoV-RBD_DMS/blob/main/results/summary/compute_binding_Kd_huACE2.md and https://github.com/tstarrlab/SARSr-CoV-RBD_DMS/blob/main/results/summary/compute_expression_meanF.md. Because most mutants in the library were independently associated with more than one N16 barcode, we derived the final mutant phenotype as the average of per-barcode measurements, as computed at: https://github.com/tstarrlab/SARSr-CoV-RBD_DMS/blob/main/results/summary/collapse_barcodes_lib40_41.md. The final per-mutant deep mutational scanning phenotypes are available at: https://github.com/tstarrlab/SARSr-CoV-RBD_DMS/blob/main/results/final_variant_scores/final_variant_scores_lib40_41.csv.

Immunogenicity

Prior to each immunization, immunogens (endotoxin-free SARS-CoV-2 HexaPro S or PRD-0038 HexaPro S) were diluted to 20 μg/mL in 1x TBS (20mM Tris, 150mM NaCl, pH 8.0) and mixed with 1:1 vol/vol AddaVax (InvivoGen vac-adx-10) to reach a final dose of 1 μg of immunogen per injection. At 8 weeks of age, 6 mice per group were anesthetized and injected intramuscularly in the quadriceps with 50μL of immunogen per leg, 100μL total at weeks 0, 3, and 6. Mice were bled via the submental route at weeks 0, 2, 5, and 8.

Blood was collected in serum separator tubes (BD # 365967) and rested for 30 min at room temperature for coagulation. Serum tubes were then centrifuged for 10 min at 2,000 x g and serum was collected and stored at -80°C until use.

Neutralization assays

For mAb neutralization against SARS-CoV-2 S VSV and PRD-0038 S K482Y/T487W VSV, HEK293T cells with stable human ACE2 expression in DMEM supplemented with 10% FBS and 1% PenStrep were seeded at 40,000 cells/well into 96-well plates [3610] (Corning) coated with poly-lysine [P4707] (Sigma) and incubated overnight at 37°C. After 16-20h of incubation, a half-area 96-well plate (Greiner) was prepared with 1:5 serial dilutions of S2X259 and S2X35 starting from 0.1 mg/ml in DMEM, and 1:3 serial dilutions of 76E1 starting from 0.5 mg/ml in DMEM, for a total of 22 μL per well. An equal volume of DMEM with diluted pseudoviruses was added to each well. All pseudoviruses were diluted between 1:3-1:27 to reach a target entry of $\sim 10^6$ RLU. The mixture was incubated at room temperature for 45-60 minutes. Media was removed from the cells and 40 μL from each well of the half-area 96-well plate containing mAb and pseudovirus were transferred to the 96-well plate seeded with cells and incubated at 37°C for 1h. After 1h, an additional 40 μL of DMEM supplemented with 20% FBS and 2% PenStrep was added to the cells. After 18–20h, 40 μL of One-Glo-EX substrate (Promega) was added to each well and incubated on a plate shaker in the dark for 5 min before reading the relative luciferase units using a BioTek Neo2 plate reader. Relative luciferase units were plotted and normalized in Prism (GraphPad): 100% neutralization being cells lacking pseudovirus and 0% neutralizing being cells containing virus but lacking mAb. Prism (GraphPad) nonlinear regression with "[inhibitor] versus normalized response with a variable slope" was used to determine IC_{50} values from curve fits with 2 technical repeats. 3 biological replicates were carried out for each mAb.

For SARS-CoV-2 D614G S VSV,[88] BA.2 S VSV, BA.5 S VSV,[75] RaTG13 S VSV,[84] and SARS-CoV-1 S VSV[111] neutralization, HEK293T cells with stable human ACE2 expression in DMEM supplemented with 10% FBS and 1% PenStrep were seeded at 40,000 cells/well into 96-well plates [3610] (Corning) coated with poly-lysine [P4707] (Sigma) and incubated overnight at 37°C. For PRD-0038 S VSV and Khosta-1 S VSV neutralization, HEK293T cells were transfected with full length *R. alcyone* ACE2 using Lipofectamine 2000 (Thermo Fisher Scientific) in Opti-MEM five hours prior to plating into 96-well plates [3610] (Corning) coated with poly-lysine [P4707] (Sigma) and incubated overnight at 37°C. The following day, a half-area 96-well plate (Greiner) was prepared with 3-fold serial sera dilutions (starting dilutions determined for each serum and pseudovirus, 22uL per well). An equal volume of DMEM with diluted pseudoviruses was added to each well. All pseudoviruses were diluted between 1:3-1:27 to reach a target entry of $\sim 10^6$ RLU. The mixture was incubated at room temperature for 45-60 minutes. Media was removed from the cells and 40 μL from each well of the half-area 96-well plate containing sera and pseudovirus were transferred to the 96-well plate seeded with cells and incubated at 37°C for 1h. After 1h, an additional 40 μL of DMEM supplemented with 20% FBS and 2% PenStrep was added to the cells. After 18–20h, 40 μL of One-Glo-EX substrate (Promega) was added to each well and incubated on a plate shaker in the dark for 5 min before reading the relative luciferase units using a BioTek Neo2 plate reader. Relative luciferase units were plotted and normalized in Prism (GraphPad): 100% neutralization being cells lacking pseudovirus and 0% neutralizing being cells containing virus but lacking sera. Prism (GraphPad) nonlinear regression with "log[inhibitor] versus normalized response with a variable slope" was used to determine ID_{50} values from curve fits with 3 technical repeats. 3 biological replicates were carried out for each sample-pseudovirus pair.

Breadth- and epitope-mapping of vaccine sera via deep mutational scanning

The complete serum deep mutational scanning pipeline is described https://github.com/tstarrlab/SARSr-CoV_MAP_PRD0038-vaccine/blob/main/results/summary/summary.md. Binding of serum was evaluated against deep mutational scanning pools for PRD-0038 and SARS-CoV-1 whose construction is described above, previously published deep mutational scanning pools for SARS-CoV-2 Wuhan-Hu-1[79] and Omicron BA.2[38], and a previously published pan-sarbecovirus panel[29] that was supplemented with additional newly described sarbecovirus and SARS-CoV-2 variants. Serum was first depleted of non-specific yeast-reactive antibodies as previously described[112]. Yeast-display RBD libraries were pooled, induced for yeast surface expression, and labeled with serum at 1:100 1:1000, 1:10,000, and 1:100,000 dilutions for one hour at room temperature. Yeast were washed with PBS-BSA and labeled with secondary Myc-FITC antibody and APC-conjugated goat anti-mouse-IgG (Jackson ImmunoResearch 115-605-008). As with ACE2-binding titrations, libraries were then partitioned into four bins of serum binding on a BD FACSAria, collecting a minimum of 6 million RBD+ cells per sample concentration across the four bins. Cells were grown post-sort, plasmid purified, N16 barcode amplified, and sequenced on an Illumina NextSeq. Raw Illumina sequencing data is available from the NCBI Sequence Read Archive, BioProject PRJNA714677, BioSample SAMN36715819. Barcode reads were mapped to library barcodes, with raw counts found at: https://github.com/tstarrlab/SARSr-CoV_MAP_PRD0038-vaccine/blob/main/results/counts/variant_counts.csv.

For each library barcode, an area under the curve (AUC) metric was derived from its distribution of sequence reads across sort bins. First, the strength of serum binding to each barcode at each serum dilution was determined as the simple mean bin from cell counts across integer-weighted bins, and subtracted by background mean bin determined from a sort from yeast libraries not incubated with sera. Any barcode with less than 3 cell counts at any sample concentration was eliminated from analysis. An AUC metric was then calculated from the relationship between mean bin and serum dilution. AUC calculation can be found at: https://github.com/tstarrlab/SARSr-CoV_MAP_PRD0038-vaccine/blob/main/results/summary/compute_AUC.md, and per-barcode AUC metrics are available at: https://github.com/tstarrlab/SARSr-CoV_MAP_PRD0038-vaccine/blob/main/results/bc_sera_binding/bc_sera_binding.csv. We then computed the per-variant AUC as the robust mean of replicate barcodes linked with the identical RBD variant, by taking the mean per-barcode AUC after trimming tails of the top and bottom 2.5% of AUC values among the replicate barcodes. Because

mutations that disrupt RBD expression artifactually decrease serum binding, we applied two final filters: first, we censored the AUC measurement for any mutant with a measured impact on RBD expression of greater than one log-MFI unit (RBD expression < -1) from DMS measurements described above; and second, we derived a normalization constant from the slope of the linear model relating serum AUC and expression globally across all library variants for variants with expression >-1, and normalized our raw AUC measurements by this constant. The final variant derivation can be found at: https://github.com/tstarrlab/SARSr-CoV_MAP_PRD0038-vaccine/blob/main/results/summary/collapse_barcodes_SARSr-DMS.md, and final per-variant serum-binding values are available at: https://github.com/tstarrlab/SARSr-CoV_MAP_PRD0038-vaccine/blob/main/results/final_variant_scores/final_variant_scores_wts.csv and https://github.com/tstarrlab/SARSr-CoV_MAP_PRD0038-vaccine/blob/main/results/final_variant_scores/final_variant_scores_dms.csv.

QUANTIFICATION AND STATISTICAL ANALYSIS

Quantification details of experiments can be found in the figure legends.